41st Aerospace Sciences Meeting and Exhibit
6-9 January 2003, Reno, Nevada

AIAA 2003-1133

NUMERICAL SIMULATION OF LEADING EDGE RECEPTIVITY OF STETSON'S MACH 8 BLUNT CONE STABILITY EXPERIMENTS

Xiaolin Zhong * **and Yanbao Ma** †
University of California, Los Angeles, California 90095

ABSTRACT

Laminar-turbulent transition in boundary layers depends on the receptivity process, which is the process of environmental disturbances initially entering the boundary layers and generating disturbance waves. The receptivity of hypersonic boundary layers to freestream disturbances is altered considerably by the presence of bow shocks in hypersonic flow fields and by the entropy layers created by the blunt noses. This paper is part II of a previous paper (AIAA paper 2002-2849) on the numerical simulation study of the receptivity to freestream acoustic disturbance waves for Mach 7.99 axisymmetric flow over a 7° half-angle blunt cone. The main focus of this study is on the excitation of the second Mack mode waves in the receptivity process in the presense of freestream acoustic waves for the case of $T' = 0$ wall boundary condition. The numerical solutions are compared with experimental results of Stetson et al. (1984) and with those obtained from a linear stability analysis. Both steady and unsteady flow solutions of the receptivity problem are obtained by computing the full Navier-Stokes equations using a high-order accurate shock-fitting finite difference scheme, which can accurately account for the effects of bow-shock/freestream-sound interactions on the receptivity process. In addition, a normal-mode linear stability analysis is also used to study the stability and receptivity properties of the boundary layer affected by the entropy layer. The most important finding of this study is that the synchronization location between mode I and the second mode plays an important role in the receptivity of the second Mack mode in the boundary layer. In the current flow over a blunt cone, the synchronization location is located downstream of the branch I neutral stability location of the second mode. As a result, there are no noticeable second mode components in the region before the synchronization location even though the second mode is linearly unstable there. Therefore mode I plays the most important role in the receptivity process, and leads to the delay of the excitation of the second mode in the current flow over a blunt cone.

INTRODUCTION

The prediction of laminar-turbulent transition in hypersonic boundary layers is a critical part of the aerodynamic design and control of hypersonic vehicles. Despite extensive studies over several decades, the mechanisms of hypersonic boundary layer stability and transition are still not well understood. Mack [1] was the first to find that there are higher acoustic instability modes in addition to the first-mode instability waves in high-Mach-number boundary layers. Among them, the second Mack mode becomes the dominant instability for hypersonic boundary layers at Mach numbers larger than about **4.** The existence and dominance of the second Mack mode has been observed by experimental studies [2,3], especially in hypersonic boundary layers over axisymmetric cones [3–7].

Stetson et al. [8] carried out boundary layer stability experiments for an axisymmetric blunt cone at Mach 7.99. The half angle of the cone is 7° and the freestream Reynolds number based on the nose radius is about 33,449. The total length of the cone is about 270 nose radii, corresponding to a Reynolds number of about 9 million. The experiments measured detailed frequency spectra of the disturbance waves along the body surface. The instability waves were found to be dominated by second Mack mode instability. There are also significant harmonic components of the second modes. They also found evidence of entropy layer instability in the region outside of the boundary layers for the case of a blunt cone with large nose radius. Stability experiments of hypersonic flow over similar geometries have also been done by other authors. Demetriades [4,5] did extensive stability experiments on hypersonic boundary layers over axisymmetric cones. Maslov and his colleagues [6,7] reported their recent stability experiments on high speed flow. Because the issue of hypersonic boundary layer stability involves many complex mechanisms, it is necessary to conduct validation studies by comparing numerical simulation results with those of stability experiments. The CFD code validation on hypersonic boundary layer transition is one of the subjects of the NATO RTO Working Group 10 [9]. The Mach 7.99, 7° blunt cone of Stetson's experiment is identified by the NATO Working Group as one of the few best available stability experiments for CFD code validation.

In the previous paper [10], we studied the receptivity

---

*Professor, Mechanical and Aerospace Engineering Department, e-mail: xiaolinOseas.ucla.edu, Associate Fellow AIAA.

† Graduate Student, Student Member AIAA

to freestream acoustic waves of the 7° half-angle blunt cone in Mach 7.99 flow, corresponding to the stability experiment by Stetson et al.[8]. The numerical simulation of the full nonlinear Navier-Stokes equations were able to take in to account the nonlinear wave interactions, the bow shock and entropy layer effects, the wall curvature effects, and the non-parallel mean flow effects on the stability of the boundary layer. The steady flow solutions of the previous paper [10] agreed very well with those computed by Esfahanian and Herbert [11] and compared well with experimental results on surface pressures and tangential velocities out side of the boundary layer. The receptivity of the Stetson's Mach 7.99 **flow** over the blunt cone to freestream fast acoustic waves was simulated by solving the full Navier-Stokes equations. The simulation results showed a complex development of wave modes induced by freestream acoustic waves. The main finding from the simulations was that the unstable second mode does not develop in the region where linear stability analysis (LST) predicts dominant unstable second modes. Instead, the second modes are excited at a later location than predicted by the LST analysis because the excitation of the second mode is governed by a different receptivity process. It was found that the synchronization location between mode I and the second mode plays an important role in the receptivity of the second Mack mode in the boundary layer. In the Mach 7.99 flow over a blunt cone, the synchronization location is located downstream of the branch I neutral stability location of the second mode. As a result, there are no noticeable second mode components in the region before the synchronization location even though the second mode is linearly unstable there. Therefore mode I and its resonant interaction with the second Mack mode plays a very important role in the receptivity process, and leads to the lack of excitation of the second mode in hypersonic flow over a blunt cone.

This paper is part II of the study presented in [10] on the numerical simulation of the receptivity of Stetson's 7° blunt cone in Mach 7.99 flow for two purposes: 1) to compare numerical results with the experimental results, and 2) more importantly, to study the detailed receptivity and stability mechanism by numerical simulations. In [10], the steady base flow was obtained by imposing an adiabatic wall boundary condition. Although the mean flow has an adiabatic wall with a zero temperature gradient on the wall, it has been generally accepted that the temperature perturbations should be set to zero because of the relatively high frequencies of the second mode. In our simulations, however, a wide range of frequencies are simultaneously imposed in the freestream. It is likely that the actual temperature perturbations may be somewhere between the two extremes of $\partial T'/\partial y_n = 0$ and $T' = 0$. Therefore, we simulate both cases of different temperature perturbations conditions on the wall with the same mean flow. The results of the test case of $\partial T'/\partial y_n = 0$ boundary condition were mainly presented in [10]. The purpose of this paper is to present the second part of the results on the receptivity for the case of using zero temperature perturbation ($T' = 0$) boundary condition. The combined results of the current paper and the previous paper [10] are expected to show a better picture of the receptivity process in hypersonic boundary layers over a blunt cone.

In the following sections, the governing equations and the receptivity simulations are briefly described. More details, along with the review of related works, can be found in part I of this work in [IO].

GOVERNING EQUATIONS AND NUMERICAL METHODS

The stability and receptivity of axisymmetric laminar hypersonic flow over a blunt cone at zero angle of attack is computed using a three-dimensional grid. The governing equations are the unsteady full three-dimensional Navier-Stokes equations written for the computation in the conservation-law form:

$$\frac{\partial U^*}{\partial t^*} + \frac{\partial F^*_j}{\partial x^*_j} + \frac{\partial F^*_{vj}}{\partial x^*_j} = 0 \qquad (1)$$

where superscript "$*$" represents dimensional variables, and

$$U^* = \{\rho^*,\ \rho^* u_1^*,\ \rho^* u_2^*,\ \rho^* u_3^*,\ e^*\}\,. \qquad (2)$$

The gas is assumed to be thermally and calorically perfect. The viscosity and heat conductivity coefficients are calculated using Sutherland's law together with a constant Prandtl number, Pr. The equations are transformed into body-fitted curvilinear computational coordinates in a computational domain bounded by the bow shock and the body surface. The location and the movement of the bow shock is an unknown to be solved for along with the flow variables by a shock-fitting method described in [12]. The unsteady bow shock shape and shock oscillations are solved as part of the computational solution. The numerical methods for spatial discretization of the 3-D full Navier-Stokes equations are a fifth-order shock-fitting scheme in streamwise and wall-normal directions, and a Fourier collocation method in the periodic spanwise flow direction for the case of a wedge geometry or in the azimuthal direction for the case of a cone geometry. The spatially discretized equations are advanced in time using Runge-Kutta schemes of up to third order.

Because the flow field behind the bow shock is not uniform, the flow variables are nondimensionalized using the freestream conditions as characteristic variables. Specifically, we nondimensionalize the velocities with respect to the freestream velocity U_∞^*, length scales with respect to the nose radius r^*, density with respect to ρ_∞^*, pressure with respect to p_∞^*, temperature with respect to T_∞^*, time with respect to r^*/U_∞^*, vorticity with respect to U_∞^*/r^*, entropy with respect to c_p^*, wave number by $1/r^*$, etc. The dimensionless flow variables are denoted by the same dimensional notation but without the superscript "*".

FLOW CONDITIONS

The flow conditions are the same as Stetson's experiments on a blunt cone, i.e.,

$$
\begin{array}{ll}
M_\infty = 7.99 & \\
p_t^* = 4 \times 10^6\, Pa & T_t^* = 750\, K \\
y = 1.4 & Pr = 0.72 \\
Re, \; = \rho_\infty^* U_\infty^* r_n^* / \mu_\infty^* = 33{,}449 &
\end{array}
$$

The viscosity is computed using the Sutherland's law for air. The cone is a $\theta = 7°$ half angle blunt cone with a spherical nose of radius: $r_n^* = 3.81 \times 10^{-3} m$. The total length of the cone is $L^* = 1.016\, m$. The corresponding Reynolds number at this length is $Re_L = 8.92 \times 10^6$. The body surface is assumed to be a non-slip wall. In the current simulations, the wall surface is assumed to be an adiabatic wall for steady base flow. As discussed in the introduction, a zero perturbation boundary condition is imposed on the wall in the unsteady flow computations.

FORCING WAVE IN RECEPTIVITY SIMULATIONS

The receptivity of an axisymmetric Mach 7.99 boundary layer to freestream waves for hypersonic flows past a 7° half angle blunt cone at zero angle of attack is considered. Following [10], initial weak forcing waves are introduced in the freestream to excite the instability waves in the boundary layer. Specifically, we simulate the receptivity process by imposing freestream acoustic disturbances according the freestream fluctuation spectra of the experiments of Stetson et al. shown in Fig. 1.

In the current study, freestream forcing disturbances are assumed to be weak planar fast acoustic waves with wave fronts normal to the center line of the body. The subsequent receptivity and development of the instability waves at these frequencies and their harmonics due to nonlinear interactions are computed by the numerical simulation. Specifically, we impose simultaneously $N = 15$ independent 2-D planar fast acoustic waves of different frequencies in the freestream. The amplitudes for each wave frequency is proportional to the wind tunnel spectra shown in Fig. *1*. The perturbation of an arbitrary flow variable can be written in the following form:

$$
q_\infty(x,y,t)' \;=\; |q'| \sum_{n=1}^{N} A_n \, e^{i[n\;\omega_1(\frac{x}{c_\infty}-t)+\phi_n]} \quad (3)
$$

where $|q'|A_n$ represents the wave amplitude of the freestream perturbation of any flow variables at a frequency

$$
w, \; = n\, w_1 \qquad (n=1,2,\cdots,N) \qquad (4)
$$

where w_1 is the minimumfrequency of the waves. The relative amplitude of each ω_n frequency is specified by A_n, which satisfies,

$$
\sum_{n}^{N} A_n^2 = 1 \qquad (5)
$$

In Eq. (3), c, is the wave speed in the freestream before reaching the shock. The initial phase angle, &, of the forcing acoustic wave at frequency ω_n is determined randomly. The absolute amplitude of the wave group is determined by setting the values of $|q'|$. For fast acoustic waves in the freestream, perturbation amplitudes of nondimensional flow variables satisfy the following dispersion relations:

$$
\begin{array}{l}
c_\infty^* = u_\infty^* + a_\infty^* \\
|\rho'|_\infty = |p'|_\infty/\gamma = |u'|_\infty M_\infty = \epsilon M_\infty; \\
|s'|_\infty = |v'|_\infty = 0
\end{array}
$$

where ϵ is a small dimensionless number representing the relative amplitude of the group of freestream acoustic waves. The forcing disturbances contain N wave frequencies which are multiples of ω_1, which are chosen such that the frequencies cover the dominant second-mode frequencies observed in the experiment.

The flow is characterized by a freestream Mach number $M_\infty = \frac{u_\infty^*}{a_\infty^*}$, and a Reynolds number defined by $Re, \; = \frac{\rho_\infty^* U_\infty^* d^*}{\mu_\infty^*}$. The forcing frequency of the freestream acoustic wave is represented by a dimensionless frequency F defined by

$$
F \;=\; 10^6\, \frac{\omega^* \nu^*}{U_\infty^{*2}} = 10^6\, \omega / Re_\infty \qquad (6)
$$

where F represents the wave frequency with respect to a viscous flow scale. We can also define a Strouhal number S using the nose radius by

$$
S \;=\; \frac{\omega^* r^*}{U_\infty^*} \qquad (7)
$$

where r^* is the nose radius. The Strouhal number represents the relative nose bluntness in the receptivity problem.

The numerical simulation for an unsteady hypersonic layer stability problem is carried out in two steps. First, a steady flow field is computed by advancing the unsteady flow solutions to convergence with no disturbances imposed. Second, unsteady viscous flows are computed by imposing freestream waves given by Eq. (3).

STEADY BASE FLOW SOLUTIONS

The steady base flow solutions of the Navier-Stokes equations for the axisymmetric Mach 7.99 flow over the blunt cone are obtained first by advancing the solutions to a steady state without forcing waves. The simulation is carried out by using a multi-zone approach using 35 zones with a total of 4200 by 121 grid points for the axisymmetric flow field from the leading edge to the 250 nose radius surface station. The corresponding Reynolds number at the 190 nose radius surface station is **6.36** x 10^6. Most of the steady solutions have been presented in the previous paper [10], where the numerical solutions were compared with Stetson's experimental results and the numerical solutions of thin-layer Navier-Stokes equations obtained by Esfahanian and Herbert [11,13]. A few additional steady flow results are presented in this paper.

Figure 2 shows the Mach number contours of the current steady state solution at about half of the computational domain near the leading edge region. In the simillation, the bow shock shape is not known in advance and is obtained as the solution for the freestream computational boundary. The results show that the Mach numbers immediately behind the bow shock approach a constant value of slightly less than 7 behind the shock at downstream locations. The locations of bow shock of the experimental measurements by Stetson et al. are marked as circular symbols in the same figure. The shapes of the two bow shocks agree very well.

The distribution of Mach numbers, pressures and temperatures immediately behind the bow shock are plotted in Figs. 3 to 5 as a function of the dimensionless x coordinates. In this paper, the origin of the x coordinates is located at the center of the nose circular surface. **A** natural coordinate s can also be used to measure the curve length of a point on the surface starting from the stagnation point. The non-dimensional s and x, normalized by the nose radius, is related to each other by the following relation:

$$x = \begin{cases} -\cos(s) & (s \leq \frac{\pi}{2} - \theta) \\ (s - \frac{\pi}{2} + \theta)\cos(\theta) - \sin(\theta) & (s > \frac{\pi}{2} - \mathbf{0}) \end{cases} \quad (8)$$

where θ is the half angle of the cone. These figures show that there is a overshoot of Mach numbers and pressures near the nose region ($x < 70$) caused by the discontinuity of surface curvatures at the junction of the spherical cone and the straight cone afterward. The flow experiences an overexpansion at the junction and goes through a recompression along the cone surface afterward. As a result, there is a slight adverse pressure gradient at downstream surface locations. At locations further downstream, the flow behind the shock approaches a constant flow of Mach number slightly less than 7.

The entropy layer was examined in [10] by studying the effect of the entropy layer on the parameter $\rho(du_t/dy_n)$, the peaks of which are the generalized inflection points. Lees and Lin [14] showed that the existence of a generalized inflection point is a necessary condition for inviscid instability in a compressible boundary layer. Stetson et al. [8] found that the peaks of $\rho(du_t/dy_n)$ associated with the generalized inflection points are difficult to detect from their experimental results. They argued that the peaks of the temperature gradients across the boundary layer, dM/dy_n, have similar locations as the generalized inflection points, but the peaks of dM/dy_n are much easier to detect from the experimental results. Therefore, they suggested the use of dM/dy_n in place of $\rho(du_t/dy_n)$ for measuring the generalized inflection points.

Figures 6 to 9 plot both $\rho(du_t/dy_n)$ and dM/dy_n side by side at four surface locations ranging from s $= 7.87$ near the leading edge to $s = 46.96$ downstream. The figures show very similar features between the two profiles and the locations of the peaks of the two profiles are very close. Again, in the region near the leading edge, there is an entropy layer outside of the boundary layer. This entropy layer is represented in a peak located initially behind the bow shock and outside of the boundary layer. In Fig. 6, the peak associated with the entropy is located approximately at $y_n = 1$. **As** the location moves downstream, this peak gradually moves towards the wall, and eventually merge with the boundary layer on the wall. In the region near the leading edge, Figs. 6 and 7 show two distinct regions in both the $\rho\frac{du_t}{dy_n}$ and dM/dy_n profiles with two separate peaks: one inside the boundary layer and another outside the boundary layer. The latter peak is created by the entropy layer. Since the generalized inflection point is located at $d(\rho du/dy_n)/dy = 0$, the additional peak outside of the boundary layer may be responsible for inviscid instability waves in the entropy layers. As s increases to 32.87 in Fig. 8, the two peaks gradually merge. Further downstream at $s = 46.96$ in Fig. 9, the peak outside of the boundary layer is absorbed by the boundary layer. After the merger, there is only one peak in the profile. Eventually, at further downstream the profiles become essentially the same as those of a sharp cone without the entropy layer effects.

RECEPTIVITY TO FREESTREAM ACOUSTIC WAVES WITH $T' = 0$ BOUNDARY CONDITION

Having obtained the steady solution, the receptivity of Stetson's Mach 7.99 flow over the 7° half-angle blunt cone to freestream acoustic waves is simulated by solving the full Navier-Stokes equations. The forcing waves are freestream planar fast acoustic waves with 15 frequencies. The unsteady flow solutions are obtained by imposing acoustic disturbances on the steady flow solutions in the freestream. The subsequent interaction of the disturbances with the shock and the receptivity of

Table 1: Acoustic wave components in the freestream.

n	f_n^* (kHz)	F_n	A_n	$\phi_n(radian)$
1	14.92	9.035	0.7692	2.4635(-6)
2	29.84	18.07	0.4162	0.1600
3	44.77	27.11	0.2827	2.2149
4	59.68	36.14	0.2065	4.1903
5	74.61	45.18	0.1707	6.0510
6	84.53	54.21	0.1406	5.2671
7	104.5	63.25	0.1132	2.1070
8	119.4	72.28	9.7164(-2)	5.7511
9	134.3	81.31	0.1081	5.0005
10	149.2	90.35	9.0781(-2)	5.2319
11	164.1	99.39	7.7722(-2)	2.1679
12	179.1	108.4	5.8428(-2)	5.4738
13	194.0	117.5	5.0729(-2)	0.5649
14	208.9	126.5	7.6987(-2)	5.5812
15	223.8	135.5	5.7108(-2)	4.4043

the boundary layer over the parabola are computed by using the full Navier-Stokes equations.

In the current test case, the freestream acoustic waves contain 15 frequencies with the lowest frequency of $f_1^* = 14.92kHz$ corresponding to dimensionless frequency of $F_1 = 9.04$, and the highest frequency of $f_{15}^* = 223.8kHz$ corresponding to dimensionless frequency of $F_{15} = 135.5$. The wave amplitudes in the freestream are set according to the experimental freestream wave spectra reported by Stetson as shown in Fig. 1. The phase angles of the waves in Eq. (3) are chosen randomly. Specifically, the wave frequencies, amplitudes, and phase angles used in the current receptivity simulation are given in Table 1. The amplitude spectrum of the acoustic waves of 15 frequencies imposed in the freestream is shown in Fig. 10 The overall wave amplitude is $\epsilon = 6.2578 \times 10^{-4}$ with 15 frequencies $(N = 15)$.

The unsteady calculations are carried out until the solutions reach a periodic state in time. Temporal Fourier analysis is carried out on local perturbations of unsteady flow variables after a time periodic state has been reached. The Fourier transform for the real disturbance functions lead to:

$$q'(x,y,t) = \Re\{\sum_{n=0}^{N} |q_n(x,y)|\, e^{i[-n\omega_1 t + \phi_n(x,y)]}\} \tag{9}$$

where $n\omega_1$ is the frequency of the n-th wave mode, $q'(x,y,t)$ represents any perturbation variables, and $|q_n(x,y)|$ and $\phi_n(x,y)$ are real variables representing the local perturbation amplitude and phase angle of the n-th wave mode. These variables indicate the amplitude of local disturbances and the local phase angle with respect to the forcing waves in the freestream. For perturbations in the boundary layer near the body surface, we can define a local growth rate α_r and a local wave number α_i of the perturbation fields by,

$$\alpha_i = \frac{1}{|q_n|}\frac{d|q_n|}{dx} \tag{10}$$

$$\alpha_r = \frac{d\phi_n}{dx} \tag{11}$$

where the derivatives are taken along a grid line parallel to the body surface.

Characteristics of Induced Waves

Figures 11 to 15 show the development of wave amplitudes of pressure perturbations for 15 forcing frequencies on the cone surface as functions of X. The lines represent 15 different frequencies of $f = nf_1$, where $f_1^* = 14.922kHz$ and $n = 1, 2, \cdots, 15$. The relative amplitudes in the freestream of waves for each frequency is set to be proportional to those of the Stetson's experiments as shown in Fig. 10.

These figures show that the receptivity process leads to a complex wave structure for disturbance waves at the forcing frequencies. As shown in later sections of this paper, the basic receptivity mechanism is the same as that of a hypersonic boundary layer over flat plate, which were studied numerically by Ma and Zhong [15] and theoretically by Fedorov [16]. For the induced waves of a given frequency, the characteristics of the induced waves undergo graduate changes from dominantly mode I waves near the leading edge to mode II waves. The second Mack mode waves can only be induced in the current receptivity process through resonance interaction with mode I wave induced by the forcing waves. The forcing acoustic waves do not directly interact with the second Mack mode. The main features of the induced waves shown in these figures are briefly described here for the purpose of demonstrating the main features of the induced waves in the boundary layer.

Figure 11 shows the amplitude development along the cone surface of the first six lower frequency waves ($n = 1, \cdots, 6$) ranging from 14.9 kHz to 84.5 kHz. It will be shown later that the induced wave growth in the boundary layer at these frequencies are not the Mack modes. They are the stable mode I waves which are induced by the forcing acoustic waves through resonant interactions. The waves developing near the leading edge in this figure are dominantly mode I waves [15]. In the case of $n = 5$, mode I waves reach a maximum value for $X \approx 117$, and decay afterward. The higher the frequency, the earlier the peaks of mode I waves will be reached. This figure also shows wave modulation for the cases of $n = 3$ and $n = 4$, consisting of components of mode I waves and the forcing acoustic waves.

Figure 12 shows the amplitude development along the cone surface of the next three frequencies ($n = 7, 8, 9$) ranging from 104.5kHz to 134.3 kHz. Again, the waves developing near the leading edge are dominantly mode I waves in the region of $X < 75$. After the decay of the mode I waves and an extended region of low wave amplitudes, the second Mack mode waves start to grow at a later surface location of $s = 180$. The second Mack mode waves do not appear in the early surface locations even though the second mode is linearly unstable there according to the linear stability analysis. For the frequency of $n = 9$, the LST analysis has shown that the second mode is unstable starting from the branch I neutral stability point located at $s = 119$. The delay in the development of the second Mack mode is consistent with Stetson's stability experiments, which also showed that the disturbances waves are not dominated by the second mode until they reach the region much downstream at 212 surface station. As shown in later sections, the generation of the second mode Mack waves is determined by the resonant interaction between mode I waves and the second Mack mode, which is not related to the branch I neutral stability of the second mode.

Figures 13 to 15 show the amplitude development along the cone surface of the higher frequency waves ($n = 10, \cdots, 15$) ranging from 149.2 kHz to 223.8 kHz. Again, the waves developing near the leading edge are dominantly mode I waves [15] in the region of $x < 75$. After the decay of the mode I waves, there are no visible second mode waves components because the second Mack mode is either stable or is very weakly unstable. Instead, the amplitude growth after the decay of mode I waves are dominantly mode II waves induced directly by the forcing acoustic waves through resonant interactions. Figure 13 also shows wave modulation for the cases of $n = 10$ and $n = 11$, consisting of components of mode II waves and the forcing acoustic waves. The wave components of $n = 16$ are also in Fig. 15. Wave modes of frequencies higher than the forcing waves are generated by nonlinear interactions among the wave modes. They are very weak in the current simulations because the receptivity is in the linear regime.

The development of wave amplitudes along the cone surface of all frequencies can be shown more clearly by the frequency spectra of surface presure perturbations, as shown in Fig. 16 for a number of surface stations ranging from 1.6 to 270 nose radius. The figure shows the spectrum of mainly three dominant wave modes induced in the boundary layer: mode I, the second Mack mode, and mode 11. At early stations, the wave modes are mainly mode I waves. At locations further downstream along the cone surface, the frequency of dominant mode I waves decreases, while mode II and second mode appears. The second Mack mode of frequencies around $130KHz$ does not appear until the waves reach 200 nose radius. The specific regions of the dominant wave modes are marked in Fig. 18. At surface location of 11 nose radius, all wave modes induced in the boundary layer are mainly mode I waves, which are linearly stable and eventually decay. At a later station of $s = 52$, the waves of lower frequencies are still dominated by mode I waves, but mode II start to develop at higher frequency waves. At the downstream location $s = 174$, the mode I wave region continues to decrease. The second mode starts to develop in the frequency around $150KHz$. There are also mode II waves at higher frequencies. At a further downstream location at $s = 274$, unsteady second Mack mode starts to develop in the frequency around $130KHz$. As the boundary layer becomes thicker at further downstream locations the dominant frequencies of the second mode decreases. There are also mode I and II waves at lower and higher frequencies, respectively.

Figures 17 and 18 show the contours of real part of temperature perturbations in the whole flow field for the frequency of $f^* = 119.4kHz$ ($n = 8$). The figures show the development of induced waves at a fixed frequency in the entire flow field, from the leading edge to downstream. In the region of $x < 20$, the figure shows that the forcing waves from the freestream passes through the bow shock and enter the boundary layer to generate mode I waves in the boundary layer. The subsequent region of $20 < x < 60$ is the develop and decay of mode I wave in the boundary layer. In the next region of $60 < x < 200$, the wave modes are a mix of forcing waves and mode I waves. The second Mach mode at this frequency starts to develop further downstream at $x > 220$ as shown in Fig. 18.

Figure 20 shows the contours of real part of temperature perturbations in a localized region of the flow field for three different modes: mode I at $f^* = 119.4kHz$ ($n = 8$), mode II at $f^* = 179.1kHz$ ($n = 12$), and the second Mack mode at $f^* = 119.4kHz$ ($n = 8$). The figure shows that mode I and II have distinctively different structure from the second Mack mode. The second mode has a typical "rope wave" structure with strong perturbation at the edge of the boundary layer, while mode I and II have stronger wave amplitudes in the boundary layer.

To summarize, the results show a complex development of wave modes induced by freestream acoustic waves. The second mode does not develop in the region where LST predicts unstable second modes to be dominant. The second modes are excited at a later location than predicted by the LST analysis. This delay may be caused by the entropy layer effects in the mean flow. The understanding of such receptivity processes may explain the fact that the nose bluntness stablizes hypersonic boundary layer flows. Therefore it is necessary to identify the wave modes in the boundary layer in the receptivity process and to identify the cause of the delay in the development of the second mode waves. The detailed LST analysis results are presented in the following sections.

Boundary-Layer Wave Mode Characteristics

The instability of hypersonic boundary layer flow over the Stetson's 7" half-angle blunt cone has been studied extensively [11,17–19] by using the normal-mode linear stability theory. However, previous LST studies have been mainly focused on the instability of the most unstable first and second-mode waves. In our previous receptivity study of Mach 4.5 boundary layer flow [”], it was found that a family of other wave modes, which are stable in a linear stability analysis, play an important role in the receptivity process. They are termed mode I, II, III, etc. in [15]. The stable wave modes generated by the forcing waves through resonant interactions can interact with the instability waves once they are generated. In order to understand the receptivity process, it is necessary to understand the characteristics of these stable wave modes in addition to the Mack modes. However, the characteristics of these stable wave modes in hypersonic flows with nose bluntness have not been well studied. Therefore, we will use the LST approach to study the wave mode properties of mode I, mode II, etc. besides the first and second Mack modes. In addition, the LST analysis is used to identify and analyze the boundary layer eigenmodes generated by forcing disturbances in the numerical simulations. Therefore, the characteristics of normal modes of the axisymmetric hypersonic boundary layer are studied by the linear stability theory in this paper.

In the studies of boundary-layer stability, the following Reynolds number, R, based on the length scale of boundary-layer thickness is often used:

$$R = \frac{\rho^*_\infty u^*_\infty L^*}{\mu^*_\infty} \tag{12}$$

where length scale of boundary-layer thickness is defined as

$$L^* = \sqrt{\frac{\mu^*_\infty s^*}{\rho^*_\infty u^*_\infty}} \tag{13}$$

where s^* is the curvature length along the wall surface measured from the leading edge. Hence, the relation between R and local Reynolds number Re, is

$$R = \sqrt{Re_s}\,. \tag{14}$$

A LST computer code based on multi-domain spectral method of Malik [20] was developed and validated by comparison with other published LST results, which were presented in our previous study [10].

Ma and Zhong [15] studied, using the linear stability theory, for boundary-layer wave mode characteristics of supersonic flow over a flat plate. It was found that the distribution of phase velocities of boundary-layer wave modes is a function of the product of the local Reynolds number $(R)$and frequency (F). Almost the same distributions of phase velocities vs $R * F$ for different boundary-layer wave modes are obtained when F is changed while R is fixed, or when R is changed while F is fixed. A similar LST study is carried out in the current study for axisymmetric hypersonic boundary-layer flow over the blunt cone. It is found that mode I and mode II are in fact “multiple-viscous solutions” by Mack [21] and by Eibler and Bestek [22]. The non-dimensional phase velocity of each normal mode can be calculated as

$$a = \frac{w}{\alpha_r}\,. \tag{15}$$

Figure 21 shows phase velocities of three discrete modes, i.e., mode I, mode II and the Mack modes, as functions of frequencies at the surface station of $s = 175$. The phase velocities of the fast acoustic wave $(1+1/M_\infty)$, entropy/vorticity wave (1), and slow acoustic wave $(1 - 1/M_\infty)$ are also shown in the figure for comparison. Both mode I and mode II originate with an initial phase velocity of the fast acoustic wave $(1+1/M_\infty)$. Before these two modes become distinct modes, their eigenvalues merge with the continuous spectra. After these two wave modes appear, their phase velocities decrease gradually with increasing w. It's obvious that it is discontinuous for the distributions of phase velocities us ω for both mode I and mode II. In the frequency spectra shown in Fig. 4 in [10], the trajectory of mode I passes across continuous spectra in the middle. In fact, mode I merges with this continuous spectra. Later, another eigenvalue from this continuous spectra becomes discrete mode I. Therefore, there is a gap in the phase velocity curve of mode I. With increasing w, the phase velocity of mode I continues to decrease and passes across the phase velocity curve of Mack modes. At the intersection point $(w = 0.1825)$, mode I is synchronized with the second Mack mode, where both modes have very similar profiles of eigenfunctions. A very similar phenomena happens to mode II at a larger ω, which is also shown in Fig. 21.

The growth rates (α_i) of different normal modes are plotted in Fig. 22. While the growth rates of Mack modes are continuous, there are two gaps in the growth rate curves for mode I and mode II. It shows that both mode I and mode II are stable modes. Mack modes are slightly unstable in the range of w between 0.0485 and 0.117. The Mack mode in this range is the conventional first mode. In the range of w between 0.171 and 0.243, the unstable Mack modes are the conventional second mode. In this range, the growth rates of the second mode change dramatically. As shown in Fig. 21 and 22, the first mode and the second mode are in fact different sections of a single mode. Here, both the first and the second mode are simply called Mack modes for convenience of discussion.

Figure **23** compares spatial growth rates for at surface station $s = 175$. The $T' = 0$ boundary condition for wall temperature perturbations is used in the current study. The experimental results of Stetson and other LST results are also plotted in the same figure for comparison. The figure shows that our results associated with an isothermal wall boundary condition compare well with other LST results that use the same wall boundary conditions. The differences between the current LST results and those of other authors are mainly due to different mean flow solutions used by different LST computations. Again, the linear stability theory predicts much higher growth rates than the experiments do. Figure 23 also shows that at the surface location of 175 nose radii, the second mode instability range is in the range between 100 kHz and 170 kHz. The first mode unstable frequency range is lower than 100 kHz.

Another important characteristic of boundary-layer unstable mode is distribution of neutral curve. Figure 24 compares the neutral curve of Mack modes with Malik's [17] results. Overall, there is good agreement between the present result and Malik's result. The difference between them is due to different mean flows used in LST analyses. The critical local Reynolds number (R) for boundary-layer instability is about 1580 ($s = 75, x = 72.5$) based on current result, which is very close to Malik's result $R = 1540 (s = 70.9, x = 68.8)$. Below this critical Reynolds number, all boundary-layer modes are stable. Figure 24 also shows that both the first mode and the second mode are stable for high frequencies above $f^* = 18Khz$.

Although mode I is stable, it was found that the stable mode I waves play an important role in the receptivity process because they interact with both the forcing acoustic waves and the unstable Mack-mode waves [15]. Through the interactions, the stable mode I waves transfer wave energy from the forcing fast acoustic waves to the second Mack-mode waves.

It should be pointed out that the discontinuous nature of mode I and mode II shown in Fig. 21 is unique to the current Mach 7.99 flow over a blunt cone. No such phenomena have been observed in our previous studies of supersonic boundary layer over a flat plate [15]. We have also been computing similar stability characteristics of planar 2-D Mach 8 flow over a 5.3° half angle sharp wedge (no nose bluntness). Figure 35 of [15] shows the distribution of phase velocities of normal modes with different frequencies for Mach 8 flow over the sharp wedge with the same freestream flow conditions. The figure shows that as ω increases, there is no discontinuity in the phase velocity of mode I and mode II when they intersect with the Mack modes. Therefore, it is conjectured that the nose bluntness introduced new characteristics in the wave phase speeds. As shown by Ma and Zhong [15], the excitation of the second mode is a result of the resonant interactions between the mode I and the freestream forcing waves. The induced mode I then interacts with the second mode when they reach the same wave speed and frequency. The discontinuity in the phase velocity in the mode I may lead to no direct interaction of mode I and the second mode. If it is true, there is no excitation of the second mode for the case of blunt cone even when the second mode is predicted by LST to be unstable.

Comparison with LST and Wave Mode Identification

In this section, the linear stability theory is used to identify different wave modes induced by fast acoustic waves. Phase velocities and structures of boundary-layer disturbances from computation of numerical simulations are compared with corresponding values from eigenvalues and eigenfunctions of the linear stability theory at the same frequency. Here, three typical frequencies with $n = 5, 8$ and 15 are chosen for the comparison. The evolution of pressure perturbations on the wall due to freestream disturbances at these three frequencies are redrawn in Fig. 25. At each frequency, the phase velocities of different wave modes are tracked from upstream to downstream by the linear stability theory. The wave structures of mode I, the second Mack mode and mode II from numerical simulations are compared with those from the linear stability theory at their respective locations.

The phase velocities of the induced boundary-layer disturbances from numerical simulations are calculated based on pressure perturbations on the wall surface by using temporal Fourier analysis according to the following formula:

$$\alpha_r = \frac{d\phi_n}{ds} \tag{16}$$

where ϕ_n is phase angle at n-th frequency from temporal Fourier analysis, and the derivatives are taken along a grid line parallel to the body surface. The value calculated by using Eqs. (16) correspond to streamwise wave number (α_r) of a single wave if the numerical solutions are dominated by a single discrete wave mode in a local region. If the numerical solutions contain a mixture of two or more wave modes, the values of streamwise wave number demonstrate the result of modulation of these mixed wave modes. At each frequency, the induced boundary-layer disturbances can be identified by comparing wavenumber and wave structures from simulations with eigenvalues and eigenfunctions obtained from the LST. Here, typical frequencies with $n = 5, 8$ and 15 are chosen for the comparison of both eigenvalues and eigenfunctions. For other frequencies, the results of comparison between DNS and LST are very similar to the results with these three typical frequencies. Therefore, only streamwise wave numbers are compared with LST results at locations with $x = 10, 50, 172$ and 272 respectively.

Figure 26 shows the distribution of the streamwise wavenumbers of the induced boundary-layer disturbances at frequency with $n = 5$ ($f^* = 74.61kHz$) from the simulation. A similar plot for the distribution of the phase velocities of boundary-layer disturbances at the same frequency is shown in Fig. 27. The real part of the eigenvalues and the phase velocities of the Mack modes and modes I from the linear stability theory are also plotted in these two figures for comparison with the numerical solutions. These figures show that there is excellent agreement in the streamwise wavenumber between the induced boundary-layer disturbances and mode I waves, which indicates that mode I waves, other than Mack mode waves are generated inside the boundary layer for this frequency.

To confirm the conclusion that mode I waves are generated in this region, profiles of induced disturbances in the numerical simulation at $x = 109.2$ are compared with mode I waves and the first-mode waves from the LST, which is shown in Fig. 28 and 29 for pressure and temperature perturbations. Here, boundary-layer disturbances are normalized by non-dimensional pressure perturbations on the wall at the location of comparison. They show that the structure of induced disturbances from the numerical simulations matches the structure of mode I wave from the LST very well inside the boundary layer (the thickness of boundary layer is about $12L$, except that there is visible difference in wave structure outside the boundary layer due to effect of forcing acoustic waves. Such agreement in wave structure between simulation results and mode I waves from the LST also exists in the comparison of other variables, which are not shown here to avoid redundancy. Meanwhile there is much difference in comparison with the first Mack mode waves. Therefore, the boundary-layer disturbances at this station are recognized as mode I waves other than the first-mode waves.

Figure 28 and 29 also shows that there is much difference in the wave structure between mode I waves and the first mode waves. While there is only one peak in real part of pressure perturbations in mode I waves, there are two peaks for the first-mode waves. Furthermore, there are very strong oscillations in profile of temperature disturbances for the first-mode waves near the edge of boundary layer, while such phenomenon does not exist in the profile of mode I waves. These characteristics of wave structure of different normal modes can be used to identify induced boundary-layer disturbances by forcing waves. It should be noted that mode I waves can only be distinguished from the first-mode waves before these two waves get synchronized with each other, where they have almost the same wave structure.

After identification of induced boundary-layer disturbances at frequency with $n = 5$ by comparison with the results of the LST, the growth and decay of induced boundary-layer disturbances shown in Fig. 25 can also be explained by using the LST. From the LST, mode I waves are always stable, which is shown in Fig. 30 for distribution of growth rates of boundary-layer normal modes. However, the induced mode I waves at frequency with $n = 5$ shown in Fig. 25 are amplified before they reach peak value of amplitude located at $x = 109.2$, which is in contradiction with the growth rates of mode I waves from the LST shown in Fig. 30.

The growth of stable mode I wave in the receptivity process can be explained from the distribution of streamwise wave number of mode I waves shown in Fig. 26 and phase velocity curve shown in Fig. 27. It shows that the wavenumber and phase velocity of mode I waves are almost same to those of fast acoustic waves near the leading edge. Due to synchronization between mode I waves and fast acoustic waves near the leading edge, mode I waves are generated by means of a resonant interaction between mode I waves inside the boundary layer and fast acoustic waves outside the boundary layer in the region upstream where wavenumber and phase velocity of mode I waves are close to those of fast acoustic waves. Though mode I is predicted to be always stable by the linear stability theory, mode I waves are strongly amplified before they reach the peak amplitude due to the resonant interaction with fast acoustic waves. The phase velocities of mode I waves decrease during the propagation downstream. When phase velocities of mode I waves decrease to a certain value and there is no more resonant interaction between mode I waves and acoustic waves, mode I waves decay due to their inherent stable properties after they reach the peak amplitude at $x = 109.2$. With the decay of mode I waves, modulation between mode I waves with acoustic waves and other waves leads to the secondary growth and decay of mode I waves with the peak amplitude located at $x = 233$ (Fig. 25). Such modulation also results in the oscillation of phase velocities further downstream, which is shown in Fig. 27.

Among different frequencies, as shown in Fig. 25, the induced boundary-layer disturbances are most strongly amplified at frequency with $n = 8$ near the exit of the computational domain. LST is used to identify the dominant normal mode included in boundary-layer disturbances at different locations. At first, the distribution of streamwise wavenumber and phase velocity of induced boundary-layer disturbances at frequency with $n = 8$ $(f^* = 119.4kHz)$ is compared with that of LST of different normal modes at the same frequency, which is presented in Figs. 31 and 32. Similar to the results shown in Fig. 21, there is a gap in the streamwise wavenumber and phase velocity curve of mode I waves from the LST. It shows that streamwise wavenumber of the induced waves are very close to those of mode I waves in the region $x < 66$, which indicates that the induced boundary-layer disturbances contain dominant mode I waves in this region. This is also confirmed by comparing wave structure with eigenfunctions of mode I waves from the LST, which is not presented here because it is very similar to the results shown in Fig. 28 and 29. In addition, the location of peak mode I waves at frequency with $n = 8$ in term of w is at 0.083 $(x = 37.1)$, which is close to the peak mode I wave location with $w = 0.087$ ($= 109.2$) for frequency with $n = 5$. This indicates some similarity in wave pattern of growth and decay of mode I waves at different frequencies when the distribution is scaled by w. Again, the resonant interaction between mode I waves inside the boundary layer and fast acoustic waves outside the boundary layer results in the amplification of the induced boundary-layer disturbances in the region with $x < 37.1$.

Meanwhile, the modulation between mode I waves and other waves, such as fast acoustic waves, and stable properties of mode I waves from the LST can explain the growth and decay of boundary-layer disturbances during their propagation downstream in the region between $37.1 < x < 190$ (Fig. 25). The wave modulation also leads to strong oscillation in boundary-layer disturbances in the same region shown in Figs. 31 and 32. At the beginning, this kind of oscillations is around the streamwise wavenumber of mode I, when the component of mode I waves included in boundary-layer disturbances is relatively strong. In the region downstream $(x > 66)$, the modulation is around the phase velocity of fast acoustic waves, which indicates the relative dominance of fast acoustic waves included in boundary-layer disturbances. In the region downstream after $x > 200$, the boundary-layer disturbances at frequency with $n = 8$ are strongly amplified as shown in Fig. 25. From distribution of streamwise wavenumber and phase velocity curves shown in in Figs. 31 and 32, the wavenumbers and phase velocities of the induced boundary-layer disturbances match those of the Mack modes in the region after $x > 250$, which shows that Mack mode waves are dominant there.

The identification of induced Mack-mode waves is confirmed by comparing the disturbance structures with the eigenfunctions of the second Mack mode from the LST at the station with $x = 271$. which is shown in Fig. 33 for pressure perturbations and 34 for temperature perturbations, respectively. Again, there is a good agreement in wave structures between the numerical simulation results and those from LST. The slight differences in the comparison is because there are other wave components, such as fast acoustic waves, included in the boundary-layer disturbances besides the second-mode waves from the numerical simulation.

After identification of the induced second Mack-mode waves inside the boundary layer, it is not difficult to understand the strong amplification of induced boundary-disturbances due to the instability of the second mode waves after they are generated by the resonant interaction with mode I. The growth rates of boundary-layer normal modes at frequency with $n = 8$ from the LST are shown in Fig. 35. At this frequency, the second-mode Branch I neutral point is located at $x = 143.4$. The second Mack-mode waves become unstable in the region after $x > 143.4$. In addition, the growth rates of the second-mode waves reach peak value $\alpha_i = -0.0051$ at $x = 234$. In other words, the second mode is most unstable and should be strongly amplified at this location. However, there are no amplified second-mode waves at frequency with $n = 8$ shown in Fig. 25 between $143.4 < x < 192$ On the contrary, the amplitude of boundary-layer disturbances slightly decays in this region. Therefore, there is still a question about how and where the second-mode waves are generated. As shown in Figs. 31 and 32, there is much difference in wavenumber curves between Mack-mode waves and fast acoustic waves. Thus, there is no direct interaction between Mack-mode waves and the forcing fast acoustic waves. Instead, there is a bridge, i.e., mode I waves, between Mack modes and fast acoustic waves. During propagation downstream, mode I waves generated by fast acoustic waves reach the synchronization point between mode I waves and Mack-mode waves located at $x = 192, \omega = 0.185$. Here, the location of synchronization point in term of w is very close to that shown in Fig. 21 with $w = 0.1825$ at the station $s/r = 175$ (or $x = 172$) where local Reynolds number R is fixed while frequency is changing. At the synchronization point, both mode I and Mack mode have very similar profiles of eigenfunctions. As a result, mode I waves convert to Mack-mode waves because Mack-mode waves are much more unstable than mode I waves from the LST, which is shown in Fig. 35. Because the second Mack-mode waves are generated by mode I waves at the synchronization point, there are no amplification of second-mode waves in the region before this point, even though the second Mack mode unstable region begins much earlier. After the generation of the second-mode waves, the boundary-layer disturbances are significantly amplified resulting from the unstable property of the second mode in the downstream region with $x > 192$, which is obviously shown in Fig. 25.

At frequency with $n = 15$, the LST results of growth rates in Fig. 36 show that all normal modes are stable. The stable property of the second mode at this frequency is also shown in Fig. 24. The streamwise wavenumbers of induced boundary-layer disturbances at frequency with $n = 15$ from the simulation are compared with the real part of eigenvalues of Mack modes, modes I and mode II from the LST, which is plotted in Fig. 37. Similarly, Fig. 38 compares the phase velocities at the same frequency from the simulation with those of the Mack modes, modes I and mode II from the linear stability theory. Once again, it shows that mode I waves are generated and amplified due to the resonant interaction between mode I waves and fast acoustic waves in the region upstream $(x < 9.5)$, where the structure of boundary-layer disturbances from the simulation can match those of mode I waves from the LST. Because the second mode is stable, there is no amplified second mode at frequency with $n = 15$ shown in Fig. 25. However, there is another wave mode which is gradually amplified during propagation downstream after $x > 50$. Figure 37 shows that this wave mode is mode II. Although mode II waves are predicted to be stable by the LST, they are strongly amplified due to the resonant interaction between mode II waves and fast acoustic waves because their streamwise wavenumber and phase velocities are very close to each other.

The wave structures of induced boundary-layer disturbances at $x = 177.3$ ($R = 2455$) from numerical simulation are compared with eigenfunctions of mode II waves from the LST at the same location, which is presented in Fig. 39 and 40. There is very good agreement in the comparison except visible difference outside the boundary layer due to acoustic waves in the simulation. Similar to mode I waves, although mode II waves are linearly stable from the LST shown in Fig. 36, there is resonant interaction between mode II waves and fast acoustic waves because their phase velocities are very close to each other as shown in Fig. 38, which leads to the amplification of mode II waves.

Having identified the dominant wave mode components included in the induced boundary-layer disturbances at the three typical frequencies, streamwise wave numbers are compared with real part of eigenvalues of different boundary-layer normal modes from the LST at the surface locations of $x = 10, 50, 172$ and 272. Such comparisons can also be used to identify the dominant wave modes for all different frequencies at these different locations. Figures 41 to 44 compare the wavenumbers of induced boundary-layer disturbances at different frequencies with LST results at these four surface locations.

At the station near the leading edge with $x = 10$, Fig. 41 shows that streamwise wavenumbers of the induced boundary-layer disturbances at different frequencies can match that of mode I waves from the LST results, which means the spectra shown in Fig. 19 are mode I waves for all different frequencies. There is better agreement in streamwise wavenumber between the simulation and the LST for low frequencies with $n \leq 11$ compared with high frequencies because the dominance of mode I waves included in boundary-layer disturbances at low frequencies. The visible difference in wavenumber curve at high frequencies with $n \geq 12$ is due to modulation of mode I waves and other wave component inside the boundary layer.

Figure 42 compares wavenumbers of induced boundary-layer disturbances at different frequencies with LST results at $/ = 52$. It shows that mode II waves are generated at high frequencies with $n = 14, 15$, while mode I waves are dominant components for lower frequencies with $n \leq 13$. The deviation of wavenumber at frequency with $n = 11$ is due to modulation of mode I waves with other modes, which is also shown in Fig. 13 where total boundary-layer disturbances at $n = 11$ decay to a minimum value at $x = 52$.

At $x = 172$, figure 43 shows that there are more mode II waves generated at high frequencies with $n \geq 12$, while mode I waves are main components in low frequency band with $n \leq 8$. In middle frequency band with $9 \leq n \leq 11$, the second Mack-mode waves are generated by mode I waves. In fact, boundary-layer disturbances at frequency with $n = 9$ at this location is in the transition region from mode I waves to the second Mack-mode waves.

Figure 44 presents comparison of wavenumbers at $/ = 272$. At this location, there are obvious second-mode waves shown in the middle frequency band between $7 \leq n \leq 10$. At frequency lower than $n = 7$, mode I waves are dominant, while mode II waves are dominant at high frequencies with $n \geq 11$.

To summarize the LST analysis of the simulation results, it is clear that the synchronization location between mode I and the second mode play the most important role in the receptivity of the second Mack mode in the boundary layer. In the current flow over a blunt cone, the synchronization location is located downstream of the branch I neutral stability location of the second mode. As a result, there are no noticeable second mode components in the region before the synchronization location even though the second mode is linearly unstable there. In addition, due to the resonant interaction with the forcing acoustic waves, there is amplification of mode I waves in the region upstream and amplification of mode II wave in the region downstream for different frequencies where all normal mode may be predicted to be stable. The delay in the excitation of the second mode in the current receptivity process leads to a delay of the second mode excitation in hypersonic boundary layers over a blunt cone.

Response coefficients

Figures 11, 12, 13, 14 and 15 show that the wave frequency has a strong effect on the boundary-layer receptivity. Because amplitudes of forcing fast acoustic waves in freestream are different at different frequencies, the frequency effect *on* the receptivity is combined with the effect of forcing-wave amplitudes in the freestream. To obtain the frequency effect on the receptivity, the induced boundary-layer disturbances characterized by pressure perturbations on the wall are normalized by amplitudes of pressure perturbations at the same frequency in freestream, which are redrawn in Figs. **45,** 46 47 and 48. Overall, amplitudes of pressure perturbations in the computational domain induced by freestream fast acoustic waves are less than **4** when they are normalized by amplitudes of freestream forcing acoustic waves. Maximum receptivity is obtained at frequency with $n = 8$ due to the growth of second-mode waves.

In the study of receptivity, a receptivity coefficient, which is defined **as** the ratio of amplitude of the induced second-mode wave at the Branch I neutral point that of the forcing freestream disturbance waves, is usually used to quantitatively describe the strength of the receptivity [23]. However, for hypersonic boundary receptivity, it is found that there are no second-mode waves generated by freestream fast acoustic waves at

Branch I neutral point because the second-mode waves are converted from mode I waves at the synchronization point between mode I and the second mode, which is located downstream of Branch I neutral stability point. Therefore, a response coefficient is defined in this paper to quantitatively study the acoustic receptivity of the boundary layer. Specifically, the response coefficient of the boundary layer to forcing disturbances for a given mode is defined as

$$K_{mode} = \frac{|p'_{mode}|}{|p'_{\infty}|} , \tag{17}$$

where $|p'|_{mode}$ is the maximum amplitude of pressure perturbations for the given wave mode. The response coefficients are used to measure the maximum responses of the relevant wave modes to forcing disturbances. For the second Mack mode, this maximum value is located at the Branch II neutral point. Since the response coefficients are not the same as the commonly used Branch I receptivity coefficient used in the literature ([23]), they are termed the response coefficients in this paper.

In the upstream region near the leading edge, the disturbance waves are dominated by mode I waves for different frequencies. Receptivity coefficients of mode I waves are obtained for frequencies with $n \leq 10$. The location of peak mode I waves moves upstream with increasing frequencies. For higher frequencies with $n \geq 11$, the locations of peak mode I waves are so close to the junction of the sphere nose and cone afterward that growth of mode I waves is contaminated by effect of discontinuity in surface curvature at the junction. Therefore, the response coefficients defined in Eqn. 17 is not available for high frequencies with $n \geq 11$. From Fig. 48, mode II waves reach local peak values for frequencies with $n = 13, 14, 15$. Meanwhile, there are no second-mode response coefficients available based on Eqn. 17 for all different frequencies. At low frequencies with $n \leq 6$, the second-mode waves will appear in the region downstream of current computational domain. Between frequency band with $7 \leq n \leq 9$, Branch II neutral points are located outside the current computational domain. For frequencies with $n = 10$ or $n = 11$, the induced second-mode waves are strongly modulated by other wave components inside the boundary layer. As a result, the peak second-mode waves are difficult to determine from the simulation results. Therefore, only response coefficients of mode I waves and mode II waves are discussed here.

Figure 49 shows the response coefficients of mode I waves and mode II waves at different frequencies. Overall, the response coefficients of mode I and mode II waves are in order of 1 for different frequencies. From our previous study on receptivity of flat-plate boundary layer to freestream fast acoustic waves [15], the response coefficients of mode I and mode II waves decrease with increasing frequencies. This trend is also true for mode I response coefficients *at* frequencies with $n \leq 7$. However, figure 49 shows that that the response coefficients of mode I waves or mode II waves increases with increasing frequencies after $n > 8$. This may be due to the effect from discontinuity at the junction in surface curvature.

SUMMARY AND CONCLUSIONS

In this paper, we have studied the receptivity of Mach 7.99 flow over a 7° half-angle blunt cone, corresponding to Stetson's stability experiments. Both the steady base flow solutions and three cases of unsteady flow solutions have been obtained and studied. The results of the test case of $\partial T'/\partial y_n = 0$ boundary condition was mainly presented in [10]. This paper presents the second part of the results on the receptivity for the case of using a zero temperature perturbation ($T' = 0$) boundary condition. Overall, the receptivity processes of the two cases have the same features. The main conclusions are:

1. The current steady flow solutions agree very well with those computed by Esfahanian and Herbert [11] and compare well with experimental results on the bow-shock shape, surface pressures and tangential velocities out side of the boundary layer. The mean flow solutions also demonstrate the effects of the entropy layer on the steady flow field.

2. The receptivity of the Stetson's Mach 7.99 flow over the blunt cone to freestream fast acoustic waves is simulated by solving the full Navier-Stokes equations. The simulation results show a complex development of wave modes induced by freestream acoustic waves. The second mode does not develop in the region where LST predicts dominant unstable second modes. The second modes are excited at a later location than predicted by the LST analysis. This delay is unique for the current flow over a blunt cone.

3. The results of LST calculations are used to identify the wave modes in the boundary layer in the receptivity process and to study the cause of the delay of the development of the second mode waves. The wave structures obtained from the simulations are compared with those obtained from the LST for mode I, mode II, and the second Mack mode. Very good agreement was obtained. The wave modes induced by the freestream acoustic waves are mode I near the nose, as it propagate downstream, second mode or mode II are excited due to the mechanism of resonant interactions between different wave modes.

4. The LST analysis shows that the synchronization location between mode I and the second mode plays an important role in the receptivity of the second Mack mode in the boundary layer. In the current

flow over a blunt cone, the synchronization location is located downstream of the branch I neutral stability location of the second mode. As a result, there are no noticeable second mode components in the region before the synchronization location even though the second mode is linearly unstable there. Therefore mode I plays the most important role in the receptivity process, and leads to the delay of the excitation of the second mode in the current flow over a blunt cone.

5. In addition, the current flow over a blunt cone also has a discontinuous phase velocity as the waves propagate downstream. Such discontinuities in the phase velocity curves may also contribute to the lack of second mode excitation.

ACKNOWLEDGMENTS

This work was sponsored by the Air Force Office of Scientific Research, USAF, under AFOSR Grant #F49620-00-1-0101, monitored by Dr. John Schmisseur. The views and conclusions contained herein are those of the author and should not be interpreted as necessarily representing the official policies or endorsements, either expressed or implied, of the Air Force Office of Scientific Research or the U.S. Government.

References

[1] Mack, L. M., "Boundary Layer Linear Stability Theory," *AGARD report, No. 709,* 1984, pp. 3–1 to 3–81.

[2] Arnal, D., "Laminar-Turbulent Transition Problems In Supersonic and Hypersonic Flows," *Special Course on Aerothermodynamics of Hypersonic Vehicles,* Vol. AGARD Report No. 761, 1988.

[3] Stetson, K. F. and Kimmel, R. L., "On Hypersonic Boundary Layer Stability," *AIAA paper 92-0737,* 1992.

[4] Demetriades, A., "Hypersonic Viscous Flow Over A Slander Cone. Part 111: Laminar Instability and Transition," *AZAA paper 74-535,* 1974.

[5] Demetriades, **A.,** "Laminar Boundary Layer Stability Measurements at Mach 7 Including Wall Temperature Effects," *AFOSR-TR-77-1311*, Vol. November, 1977.

[6] Maslov, A. A., Shiplyuk, A. N., Sidorenko, A., and Arnal, D., "Leading-edge receptivity of a hypersonic boundary layer on a flat plate," *Jounral of Fluid Mechanics,* Vol. 426, 2001, pp. 73–94.

[7] Maslov, **A.** A., Mironov, S. G., and Shiplyuk, A. **A.,** "Hypersonic Flow Stability Experiments," *AZAA Paper 2002-0153, 2002.*

[8] Stetson, K. F., Thompson, E. R., Donaldson, J. C., and Siler, L. G., "Laminar Boundary Layer Stability Experiments on a Cone at Mach 8, Part 2: Blunt Cone," *AIAA paper 84-0006*, January 1984.

[9] Schneider, S. P., "Hypersonic Laminar Instability on Round Cones Near Zero Angle of Attack," *AIAA Paper 2001-0206,* 2001.

[10] Zhong, X. and Ma, *Y.*, "Receptivity and Linear Stability of Stetson's Mach 8 Blunt Cone Stability Experiments," *AZAA Paper 2002-2849,* January 2002.

[11] Herbert, T. and Esfahanian, V., "Stability of Hypersonic Flow over a Blunt Body," *AGARD CP-514*, Vol. pp. 28-1 – 12, April, 1993.

[12] Zhong, X., "High-Order Finite-Difference Schemes for Numerical Simulation of Hypersonic Boundary-Layer Transition," *Journal of Computational Physics*, Vol. 144, August 1998, pp. 662–709.

[13] Esfahanian, V., *Computation and stability analysis of laminar flow over a blunt cone in hypersonic flow*, Ph.D. thesis, The Ohio State University, 1991.

[14] Lees, L. and Lin, C. C., "Investigation of the Stability of the Laminar Boundary Layer in Compressible Fluid," *NACA TN No. 1115,* 1946.

[15] Ma, *Y.* and Zhong, X., "Receptivity to Freestream Disturbances of Mach 4.5 Flow over A Flat Plate," *AIAA Paper 2002-0140*, January 2002.

[16] Fedorov, A. V. and Khokhlov, A. P., "Prehistory of Instability in a Hypersonic Boundary Layer," *Theoretical and Computational **Fluid** Dynamics,* Vol. 14, 2001, pp. 359–375.

[17] Malik, M. R., Spall, R. E., and Chang, C.-L., "Effect of Nose Bluntness on Boundary Layer Stability and Transition," *AIAA paper 90-0112*, 1990.

[18] Kufner, E., Dallmann, U., and Stilla, J., "Instability of Hypersonic Flow Past Blunt Cones – Effects of Mean Flow Variations," *AIAA paper 93-2983*, June 1993.

[19] Kufner, E. and Dallmann, U., "Entropy- and Boundary Layer Instability of Hypersonic Cone Flows – Effects of Mean Flow Variations," *IUTAM Symposium on Laminar-Turbulent Transition,* Vol. Sendai/Japan, September 1994, pp. 197-204, Springer-Verlag, Berlin, 1994.

[20] Malik, M. R., "Numerical Methods for Hypersonic Boundary Layer Stability," *Journal of Comp. Phys.*, Vol. 86, 1990, pp. 376–413.

[21] Mack, L. M., "Stability of Axisymmetric Boundary Layers on Sharp Cones at Hypersonic Mach Numbers," *AIAA Paper* 87-1413, 1987.

[22] Eibler, W. and Bestek, H., "Spatial Numerical Simulations of Linear and Weakly Nonlinear Instabilities in Supersonic Boundary Layers," *Theoretical and Computational Fluid Dynamics*, Vol. *8*, 1996, pp. 219–235.

[23] Saric, W. S., Reed, H. L., and Kerschen, E. J., "Boundary-Layer Receptivity to Freestream Disturbances," *Annual Review* of *Fluid Mechanics*, Vol. 34, 2002, pp. 291–319.

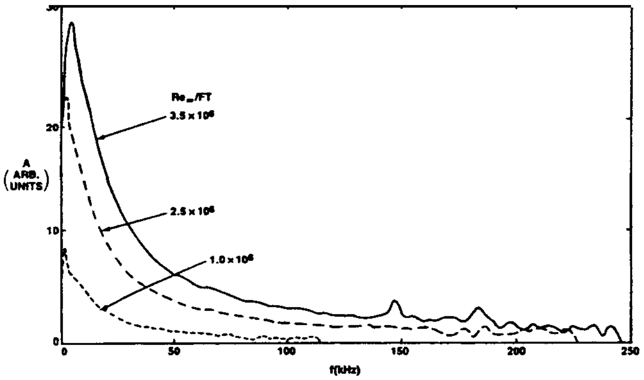

Figure 1: Freestream disturbance spectra in Stetson et al.'s experiments (1984).

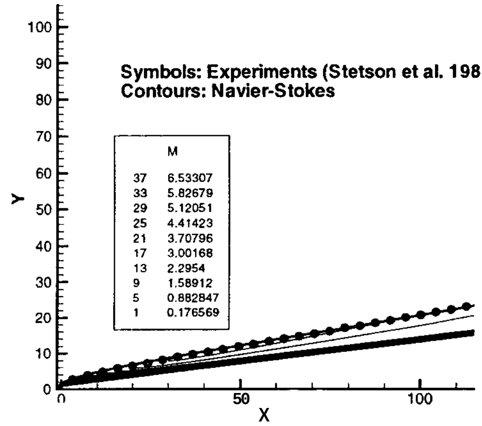

Figure 2: Mach number contours for steady Mach 7.99 flow over a 7° half-angle blunt cone. The experimental bow shock shape (Stetson et al., 1984) is compared with the current numerical solutions.

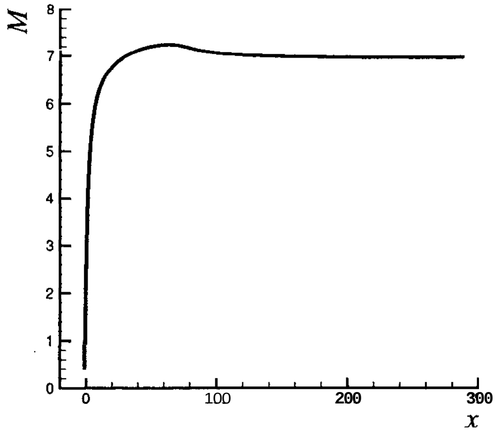

Figure **3:** The distribution of Mach numbers immediately behind the bow shock.

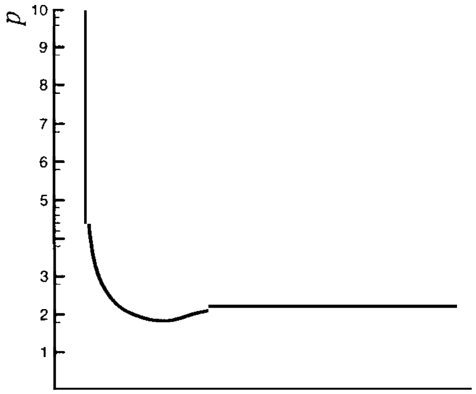

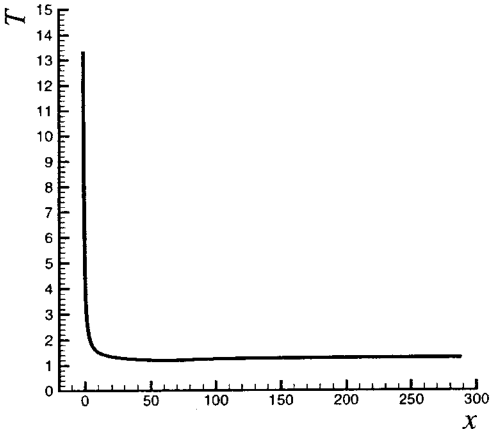

Figure 5: The distribution of temperature immediately behind the bow shock.

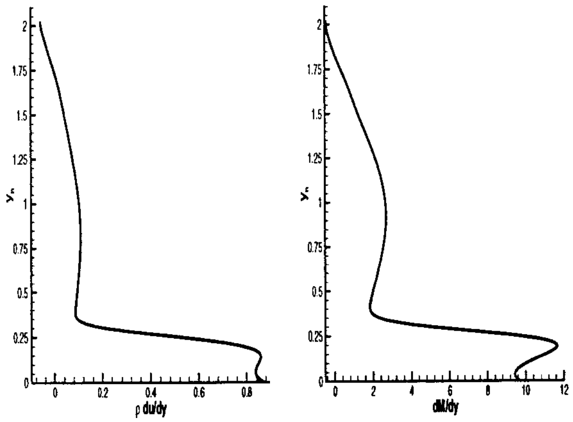

Figure 6: The profiles of $\rho\frac{du_t}{dy_n}$ and $\frac{dM}{dy_n}$ along the wall-normal direction at the surface location of s = 7.87 nose radii.

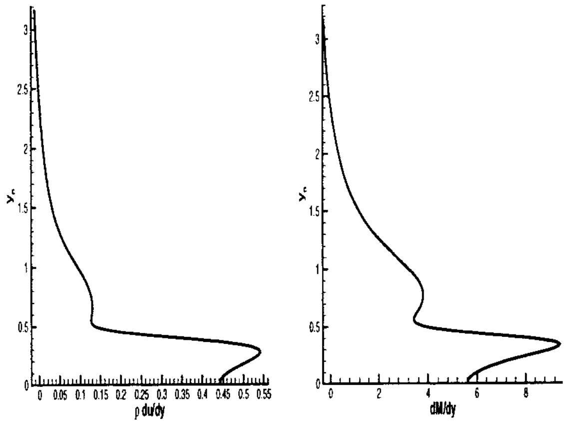

dM

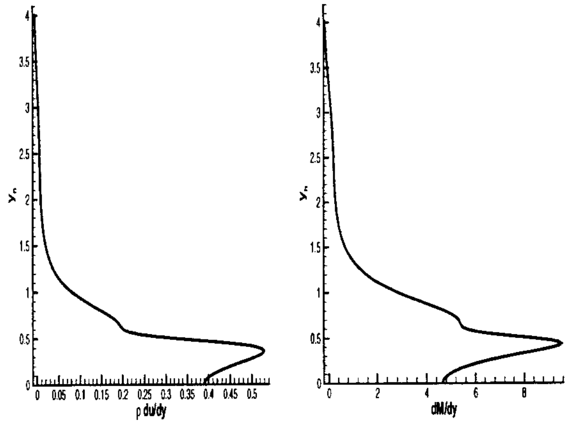

Figure 8: The profiles of $\rho\frac{du_t}{dy_n}$ and $\frac{dM}{dy_n}$ along the wall-normal direction at the surface location of s = **32.87** nose radii.

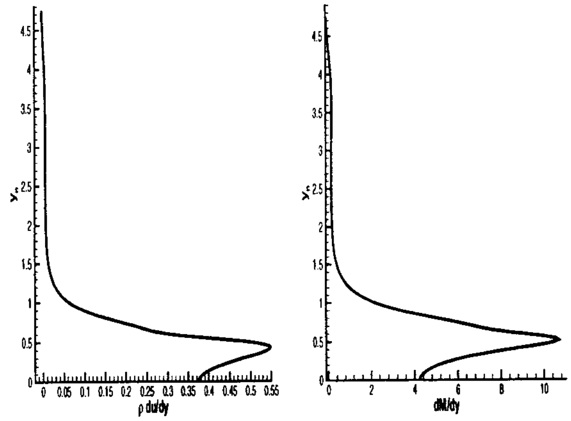

Figure 9: The profiles of $\rho\frac{du_t}{dy_n}$ and $\frac{dM}{dy_n}$ along the wall-normal direction at the surface location of s = 46.96 nose radii.

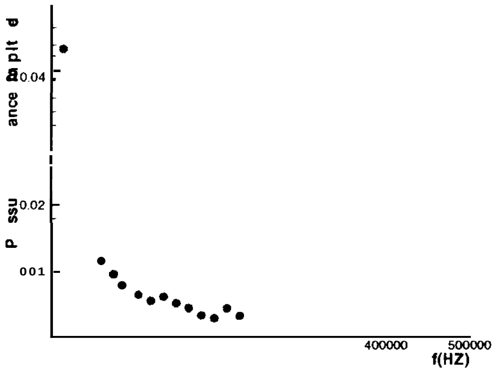

Figure 10: The frequency spectrum of the pressure perturbations imposed in the freestream in the numerical simulations.

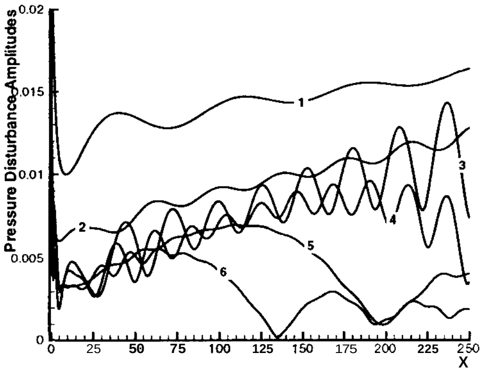

Figure 11: Amplitudes of pressure perturbations on the cone surface vs. /. The lines represent 6 different frequencies of $f_n = nf_1$, where $f_1^* = 14.922kHz$ and $n = 1, 2, \cdots, 6$.

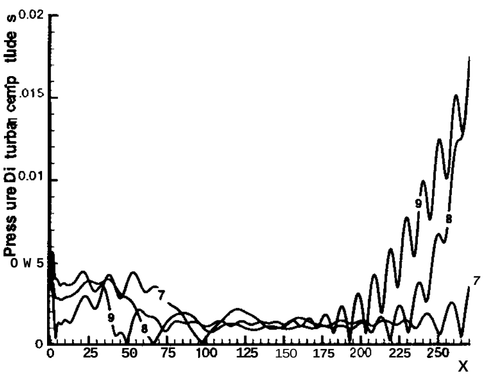

Figure 12: Amplitudes of pressure perturbations on the cone surface vs. x. The lines represent 3 different frequencies of $n = 7, 8, 9$.

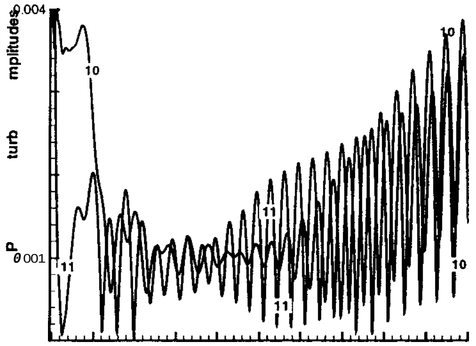

Figure 13: Amplitudes of pressure perturbations on the cone surface vs. x. The lines represent 2 different frequencies of $n = 10, 11$.

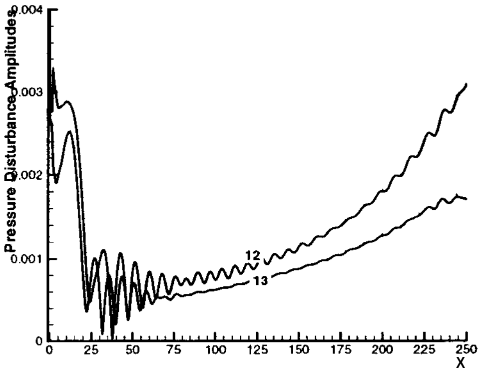

Figure 14: Amplitudes of pressure perturbations on the cone surface vs. /. The lines represent 2 different frequencies of $n = 12, 13$.

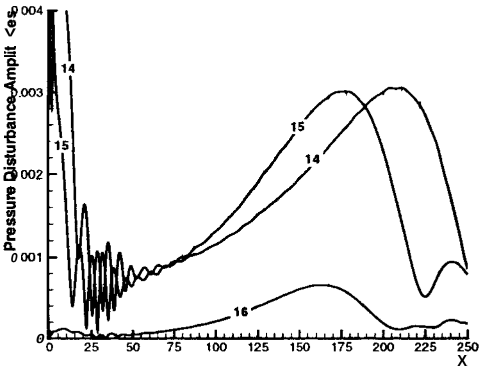

Figure 15: Amplitudes of pressure perturbations on the cone surface vs. x. The lines represent 3 different frequencies of $n = 14, 15, 16$.

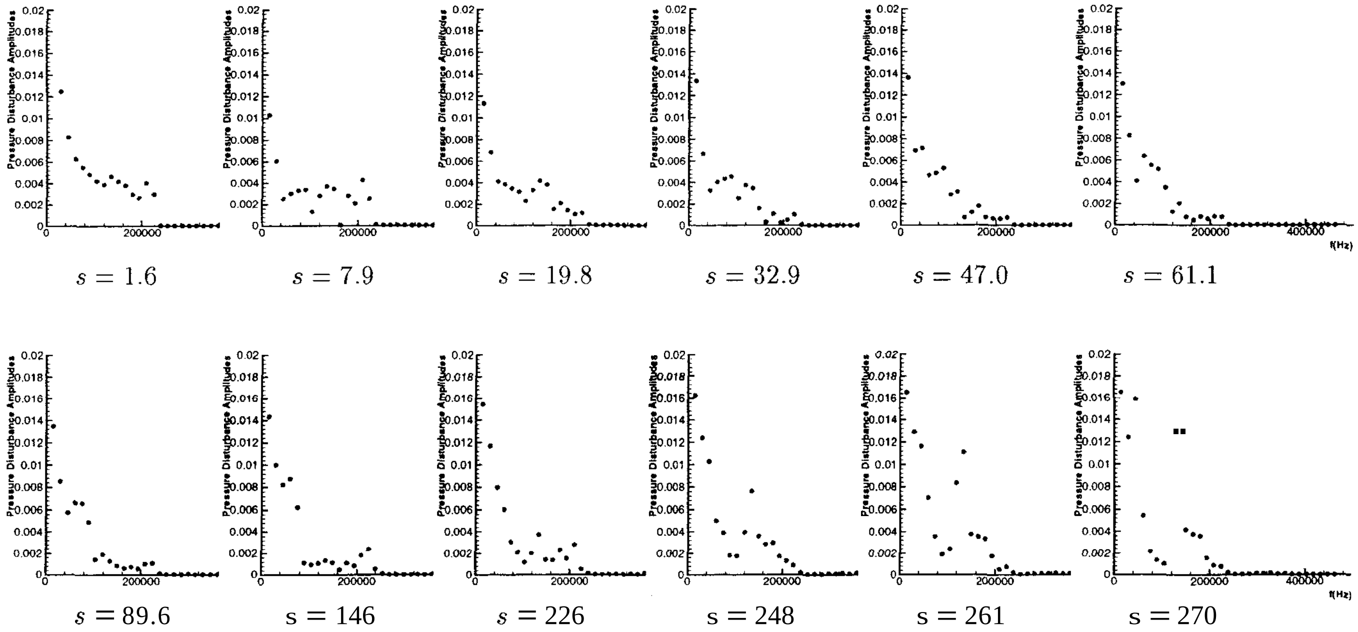

$s = 1.6$ $s = 7.9$ $s = 19.8$ $s = 32.9$ $s = 47.0$ $s = 61.1$

$s = 89.6$ s = 146 $s = 226$ s = 248 s = 261 s = 270

Figure 16: The frequency spectrum of the pressure perturbations on the cone surface at a number of surface locations.

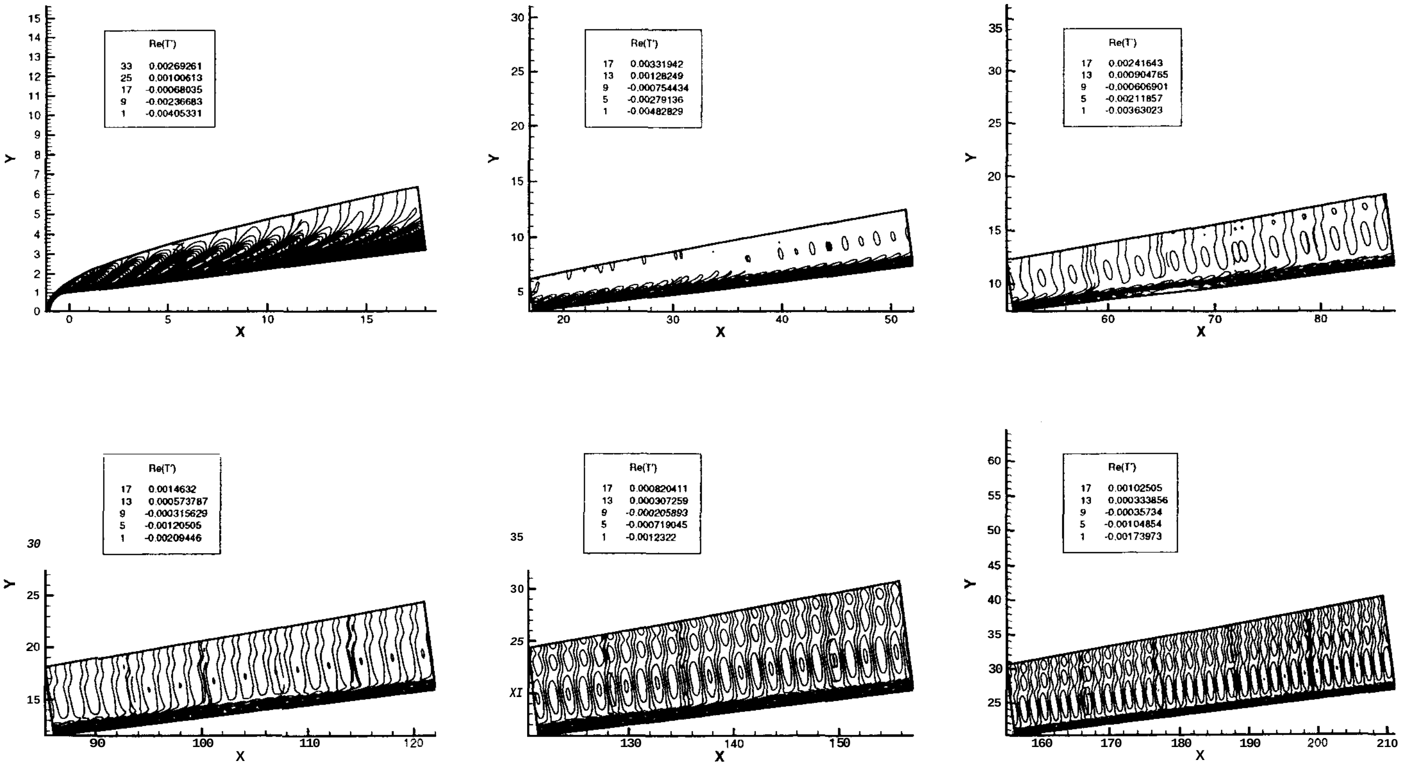

Figure 17: Contours of real part of temperature perturbations in the flow field for the frequency of $f' = 119.4kHz$ $(n=8)$.

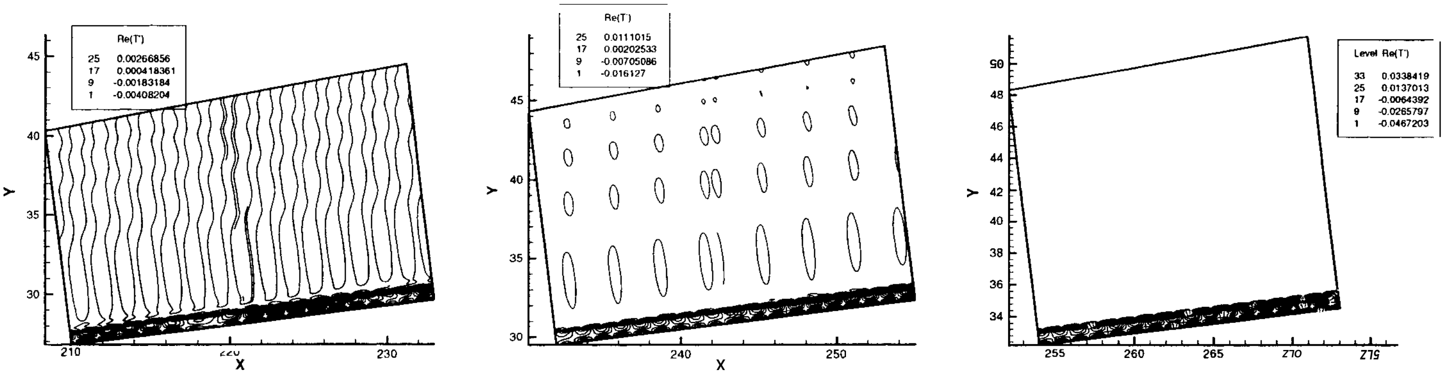

Figure 18: Contours of real part of temperature perturbations in the flow field for the frequency of $f^* = 119.4kHz$ $(n = 8)$.

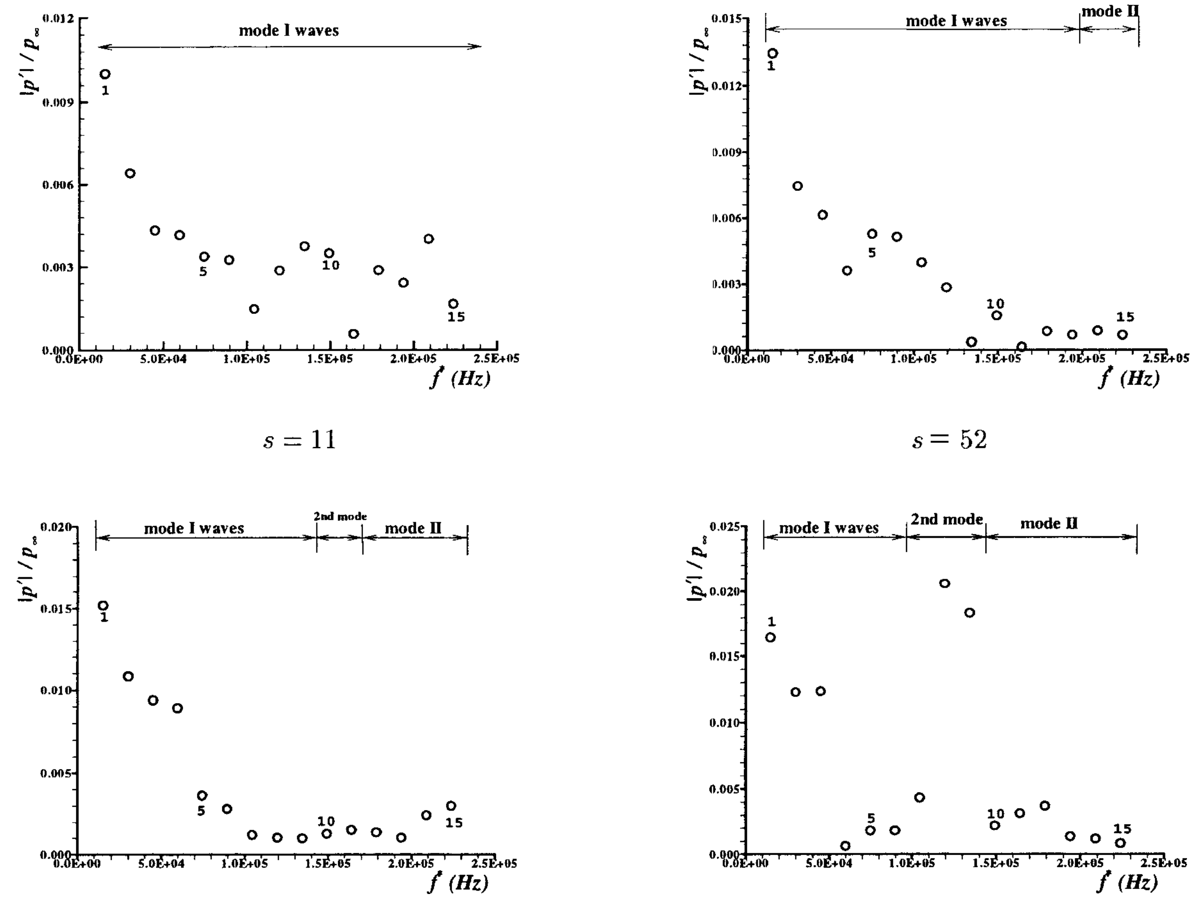

$s = 11$

$s = 52$

$s = 174$

$s = 274$

Figure 19: The frequency spectrum of the pressure perturbations on the cone surface at a number of surface locations.

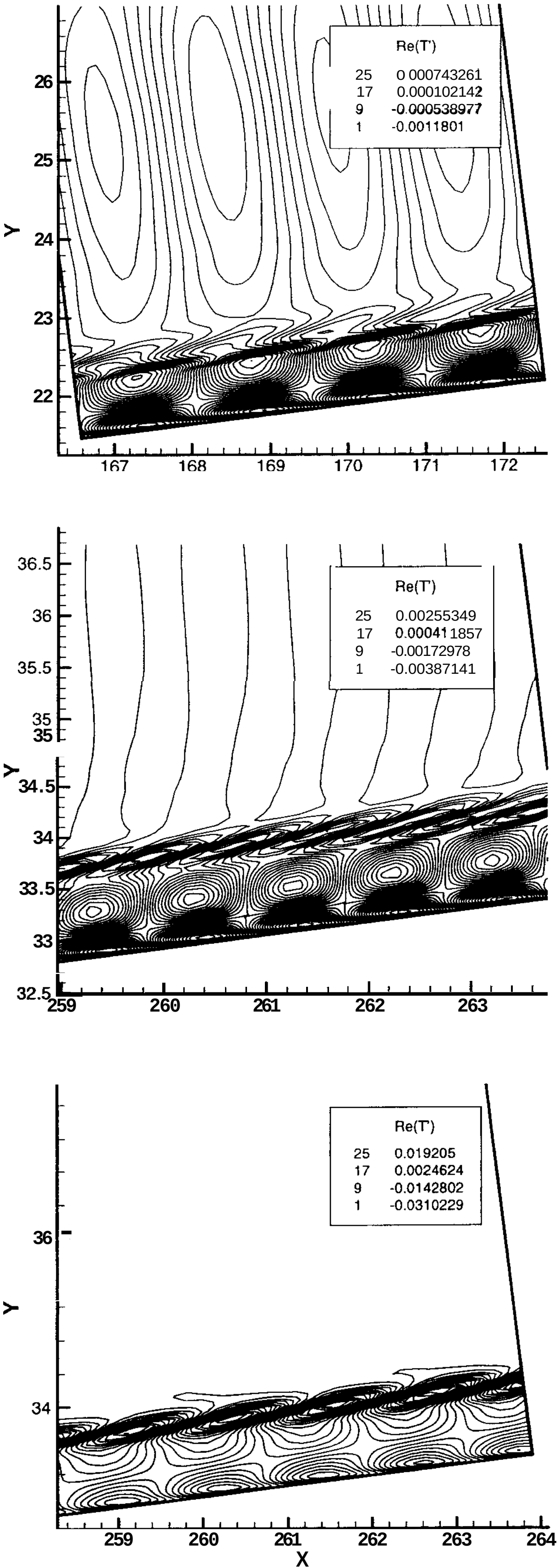

Figure 20: Contours of real part of temperature perturbations in a localized region of the flow field for three different modes: top figure, mode I at $f^* = 119.4kHz$ $(n = 8)$; mid figure, mode II at $f^* = 179.1kHz$ $(n = 12)$; bottom figure, second **Mack** mode at $f^* = 119.4kHz$ $(n = 8)$.

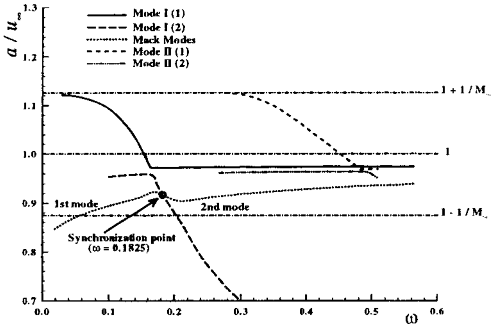

Figure 21: Phase velocities of three discrete modes, i.e., mode I, mode II and the Mack modes, changing with frequencies at the station $s = 175$.

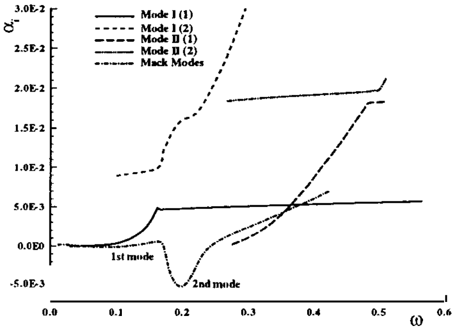

Figure 22: Growth rates of three discrete modes, i.e., mode I, mode II and the Mack modes, changing with frequencies at the station $s = 175$.

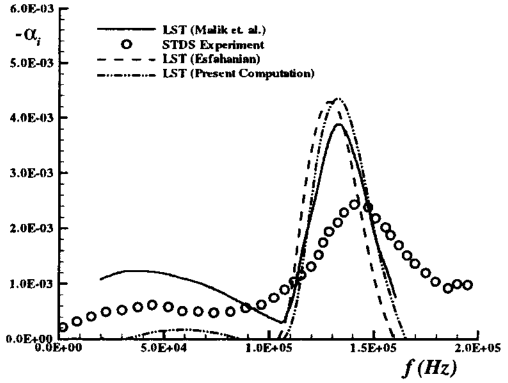

Figure 23: Comparison of disturbance growth rates predicted by LST and experiments at $s = 175$ ($x = 172$).

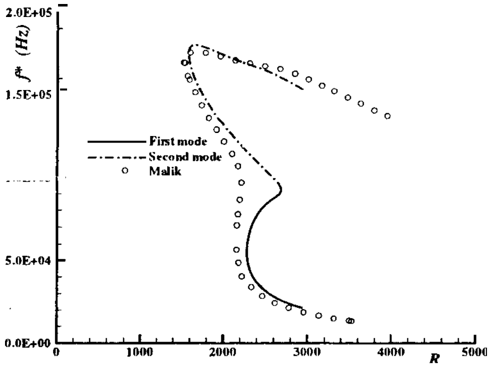

Figure **24:** Comparison of the neutral curve of Mack modes with Malik's (1990) results.

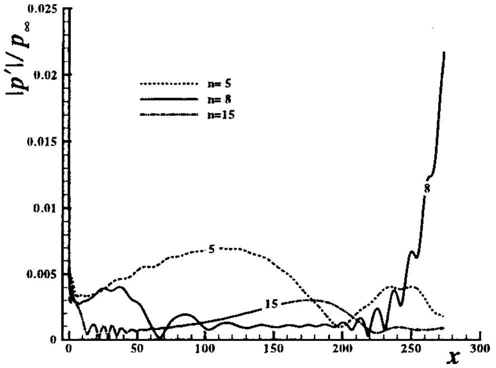

Figure 25: The evolution of pressure perturbations on the wall due to freestream disturbances at three frequencies.

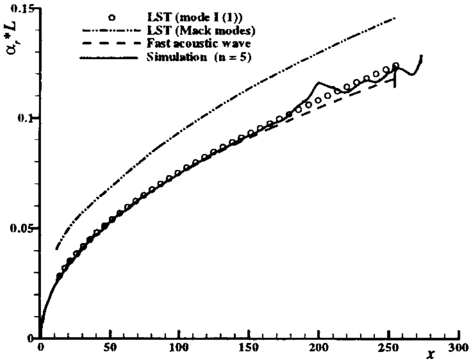

Figure 26: The distribution of the streamwise wavenumber of induced boundary-layer disturbances at frequency with $n = 5$ ($f^* = 74.61kHz$) from the simulation.

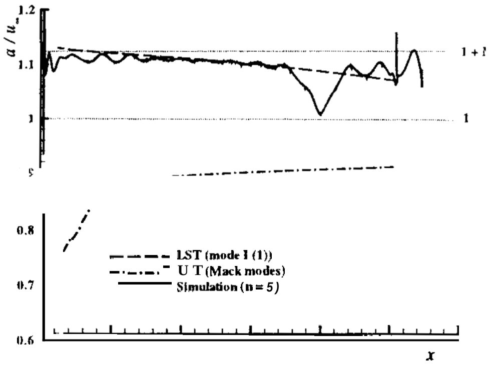

Figure 27: Comparison of phase velocity of induced boundary-layer disturbances at frequency with $n = 5$ (f* $= 74.61kHz$) from the simulation with that of boundary-layer normal modes from the LST.

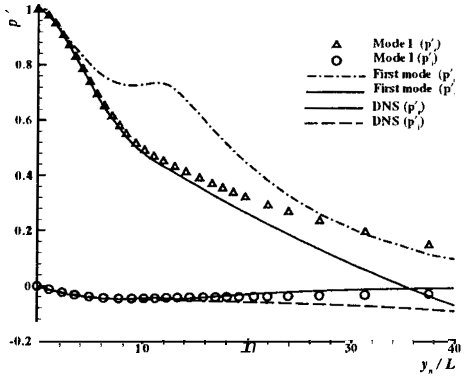

Figure 28: Profiles of induced disturbances in the numerical simulation at $x = 109.2$ compared with mode I waves and the first-mode waves from the LST.

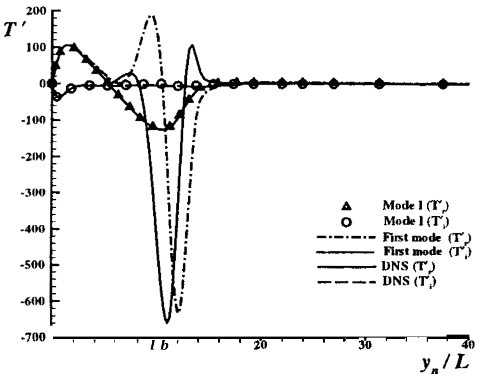

Figure 29: Profiles of induced disturbances in the numerical simulation at $x = 109.2$ compared with mode I waves and the first-mode waves from the LST.

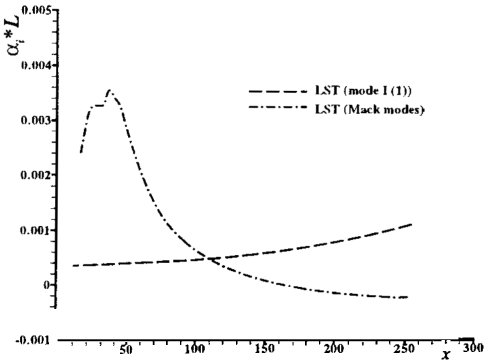

Figure **30:** Distribution of growth rates of boundary-layer normal modes at frequency with $n = 5$.

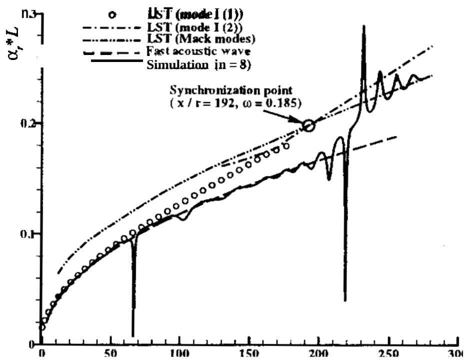

Figure **31:** The distribution of the streamwise wavenumber of induced boundary-layer disturbances at frequency with $n = 8$ $(f^* = 119.4kHz)$ from the simulation.

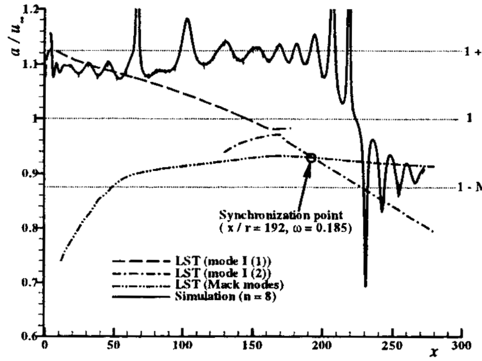

Figure **32:** Comparison of phase velocity of induced boundary-layer disturbances at frequency with $n = 8$ $(f^* = 119.4kHz)$ from the simulation with that of boundary-layer normal modes from the LST.

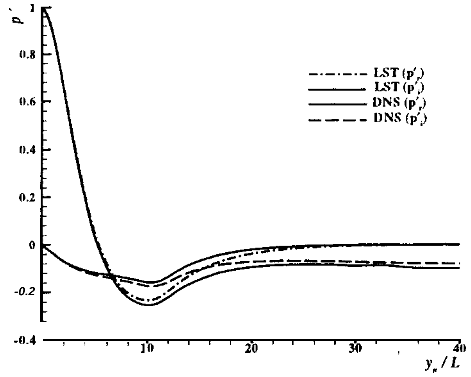

Figure *33:* Profiles of induced disturbances in the numerical simulation at $X = 271$ compared with the second Mack mode waves from the LST (n = 8).

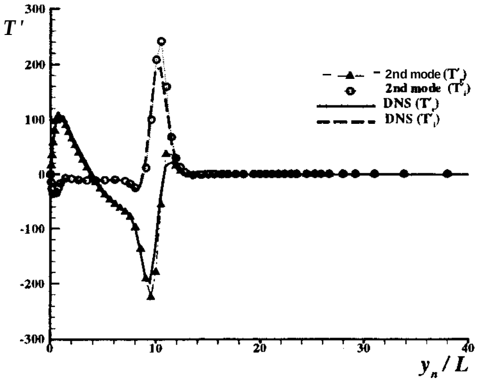

Figure **34:** Profiles of induced disturbances in the numerical simulation at $X = 271$ compared with the second Mack mode waves from the LST (n = 8).

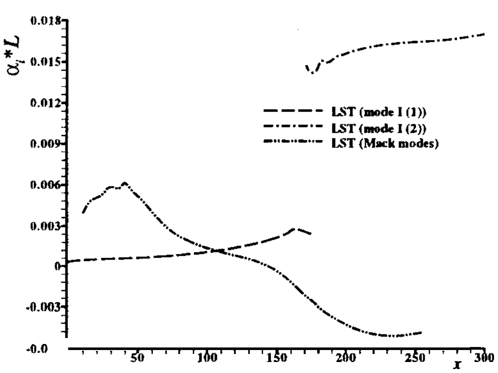

Figure 35: Distribution of growth rates of boundary-layer normal modes at frequency with $n =$ \$.

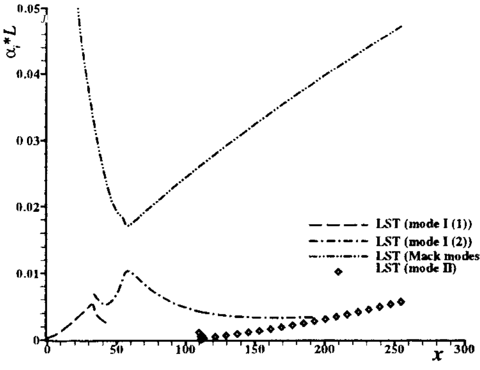

Figure **36:** Distribution of growth rates of boundary-layer normal modes at frequency with $n = 15$.

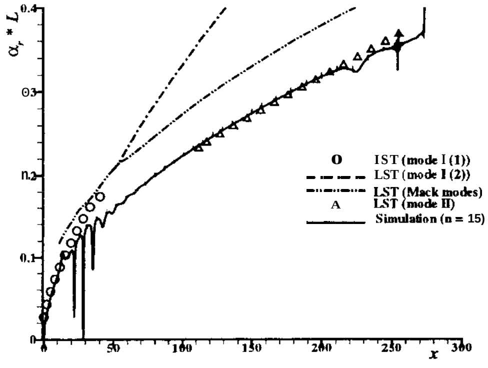

Figure 37: The distribution of the streamwise wavenumber of induced boundary-layer disturbances at frequency with $n = 15$ $(f^* = 223.8kHz)$ from the simulation.

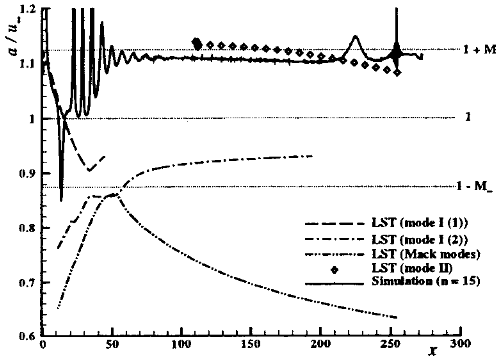

Figure 38: Comparison of phase velocity of induced boundary-layer disturbances at frequency with $n = 15$ $(f^* = 223.8kHz)$ from the simulation with that of boundary-layer normal modes from the LST.

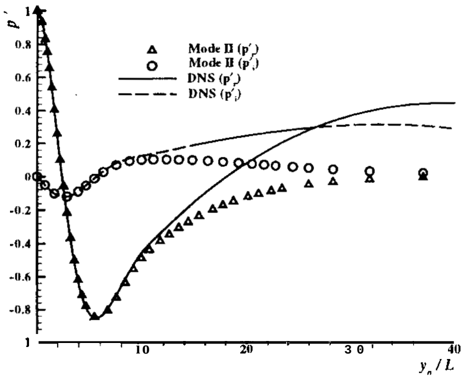

Figure 39: Profiles of induced disturbances in the numerical simulation at $x = 177.3$ compared with the second-mode waves from the LST (n = 15).

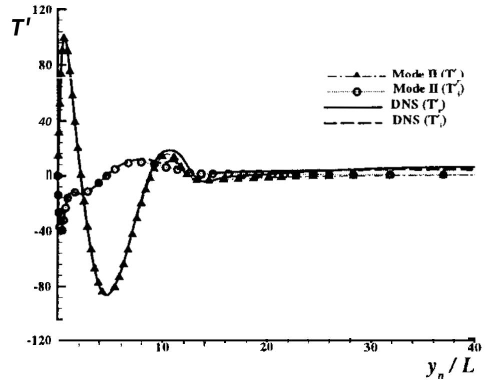

Figure 40: Profiles of induced disturbances in the numerical simulation at $x = 177.3$ compared with the second-mode waves from the LST (n = 15).

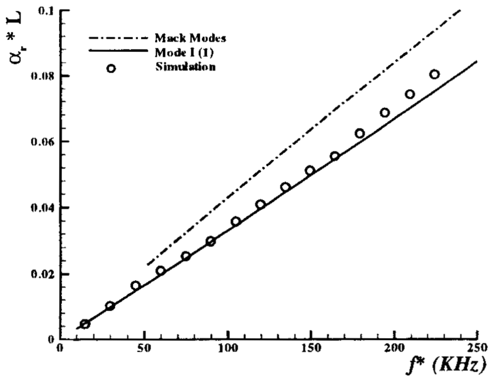

Figure 41: Comparison of wavenumbers of induced boundary-layer disturbances at different frequencies with LST results at $x = 10$.

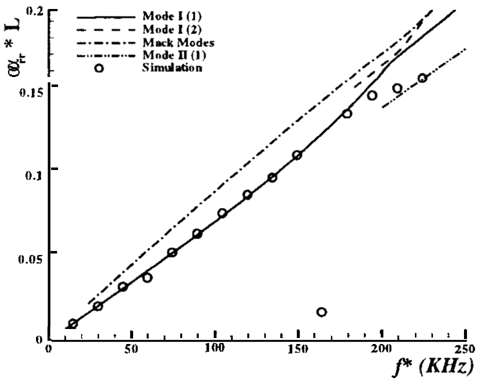

Figure 42: Comparison of wavenumbers of induced boundary-layer disturbances at different frequencies with LST results at $x = 52$.

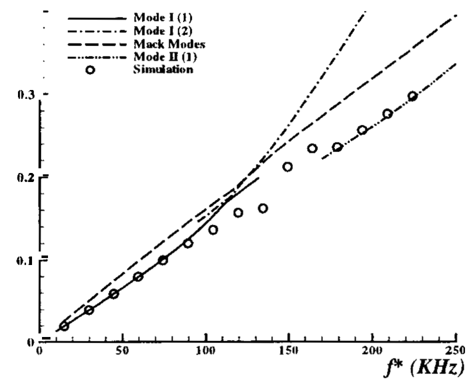

Figure 43: Comparison of wavenumbers of induced boundary-layer disturbances at different frequencies with LST results at $x = 175$.

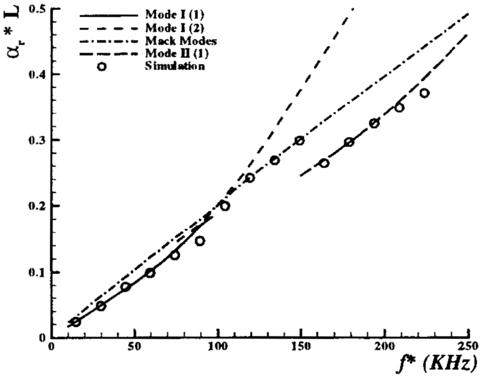

Figure **44**: Comparison of wavenumbers of induced boundary-layer disturbances at different frequencies with LST results at $x = 272$.

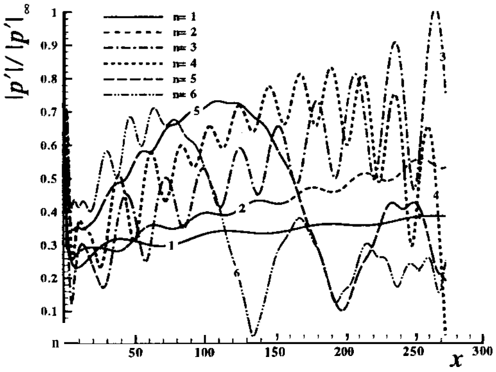

Figure 45: Pressure perturbations on the wall normalized by amplitudes of pressure perturbations at the same frequency in freestream.

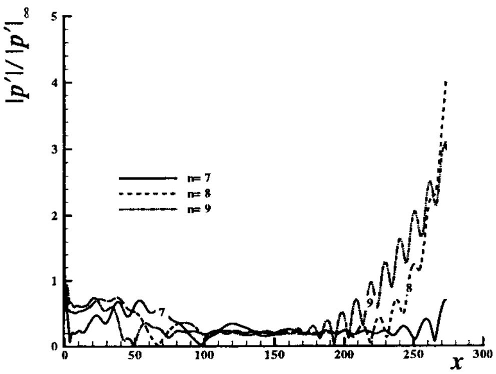

Figure 46: Pressure perturbations on the wall normalized by amplitudes of pressure perturbations at the same frequency in freestream.

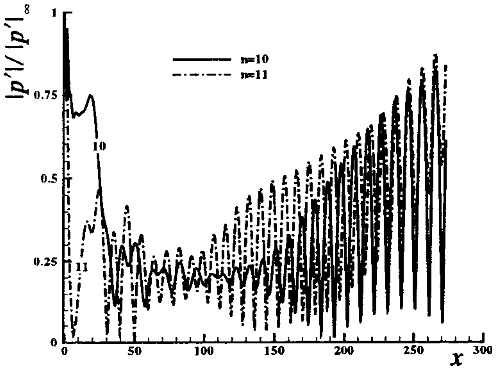

Figure **47:** Pressure perturbations on the wall normalized by amplitudes of pressure perturbations at the same frequency in freestream.

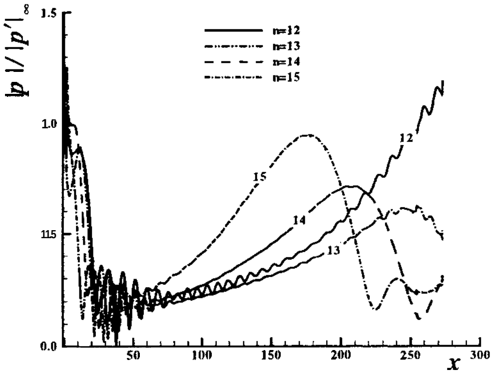

Figure 48: Pressure perturbations on the wall normalized by amplitudes of pressure perturbations at the same frequency in freestream.

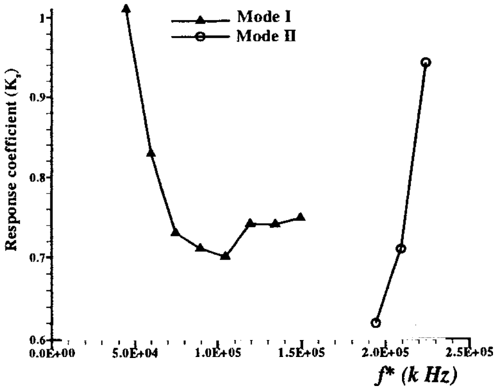

Figure 49: The response coefficients of mode I waves and mode II waves at different frequencies.